Johann Radon Institute for
Computational and Applied Mathematics
Austrian Academy of Sciences (ÖAW)

A Mumford-Shah level-set approach for the inversion and segmentation of SPECT/CT data

E. Klann, R. Ramlau, W. Ring

RICAM-Report 2009-06

A MUMFORD-SHAH LEVEL-SET APPROACH FOR THE INVERSION AND SEGMENTATION OF SPECT/CT DATA

ESTHER KLANN*, RONNY RAMLAU†, AND WOLFGANG RING‡

Abstract. This paper presents a level-set based approach for the simultaneous reconstruction and segmentation of the activity as well as the density distribution from tomography data gathered by an integrated SPECT/CT scanner.

Activity and density distributions are modelled as piecewise constant functions. The segmenting contours and the corresponding function values of both the activity and the density distribution are found as minimizers of a Mumford-Shah like functional over the set of admissible contours and – for fixed contours – over the spaces of piecewise constant density and activity distributions which may be discontinuous across their corresponding contours. For the latter step a Newton method is used to solve the nonlinear optimality system. Shape sensitivity calculus is used to find a descent direction for the cost functional with respect to the geometrical variabla which leads to an update formula for the contours in the level-set framework. A heuristic approach for the insertion of new components for the activity as well as the density function is used. The method is tested for synthetic data with different noise levels.

1. Introduction

Tomography is a widely used technique in medical imaging. SPECT/CT is a hybrid imaging technique enabling a direct correlation of anatomical information from CT (Computerized Tomography) and functional information from SPECT (Single Photon Emission Computerized Tomography) [3, 4, 14]. An integrated SPECT/CT scanner gathers both the CT data set and the SPECT data set in one procedure with the patient in the same position. Hence, it allows a precise overlay of the gathered information. In contrast, for reconstructions from separately obtained CT and SPECT acquisitions one always has to deal with motion artefacts, which can markedly affect the overlay of the sought-after functional and anatomical information. We start with a brief sketch of the underlying physical phenomena and the mathematical modeling of the considered tomographic techniques.

Computerized Tomography (CT) is used to get information on the morphology of a sample, e.g., in medical imaging a human body or in nondestructive testing a workpiece. For this, the *mass density distribution* μ of the sample is determined from measurements of the attenuation of x-ray

Date: March, 3rd 2009.

1991 *Mathematics Subject Classification.* 34K29, 44A12, 49M05, 65K10, 92C50, 94A08.

Key words and phrases. level set method, shape sensitivity analysis, tomography, active contours, Mumford-Shah functional, inverse problems.

The Work of E. Klann was funded by FWF-project P19029-N18.

beams sent through the material from different angles and offsets. The measured data z are connected to the body density μ via the *Radon transform*,

$$z(s,\omega) \sim R\mu(s,\omega) = \int_{\mathbb{R}} \mu(s\omega + t\omega^{\perp})\, dt \ , \tag{1.1}$$

$(s,\omega) \in \mathbb{R} \times S^1$, see [35]. To compute the density distribution μ, the equation $R\mu = z$ has to be inverted. Whereas CT provides structural information, Single Photon Emission Computerized Tomography (SPECT) is an imaging method designed to provide information about the *functional level* of a part of the body. SPECT involves the injection of a low-level radioactive chemical, called radiotracer or *radiopharmaceutical* into the bloodstream. The radiotracer travels in the bloodstream and accumulates, e.g., in the heart or it can be attached to certain types of proteins which are known to bind to tumor cells. The concentration of the radiopharmaceutical within the body is referred to as *activity distribution* f. The radioactive material ejects photons which travel through the body and interact with the tissue, modelled as density function μ. Finally the photons are measured outside the body by a SPECT scanner (a γ-camera). The resulting sinogram data y is modelled by the *attenuated Radon transform*,

$$y(s,\omega) \sim A(f,\mu)(s,\omega) = \int_{t\in\mathbb{R}} f(s\omega + t\omega^{\perp}) \exp\left(-\int_{\tau=t}^{\infty} \mu(s\omega + \tau\omega^{\perp})\, d\tau\right) dt \ , \tag{1.2}$$

$(s,\omega) \in \mathbb{R} \times S^1$.

We discuss some properties of the Radon and the attenuated Radon transform as well as some solution methods for CT and SPECT. The Radon transform (1.1) is a linear operator which is bounded as operator from the Sobolev space $H^s(\Omega)$ into the Sobolev space $H^{s+1/2}(S^1 \times \mathbb{R})$ and for this case an inversion formula exists [35]. As an operator between L_2-spaces the Radon transform is compact and the problem of solving $R\mu = z$ from measured data z^δ is ill-posed, hence the Radon inversion formula does not yield accurate results and regularization methods have to be applied. Probably the most widely used algorithm for the inversion of x-ray tomography data is the filtered backprojection method [40, 47].

The attenuated Radon transform (1.2) is linear with respect to the first argument – the activity f – and non-linear with respect to the second argument, the density μ. There are several approaches to solve (1.2): For known density distribution μ the problem reduces to the linear operator equation $A_\mu f = y$ and only f is to be determined from the measurements y. This describes one standard way of dealing with the SPECT problem: it is assumed that the density μ is known, e.g., from an additional CT scan as solution of the Radon problem. For the linear attenuated Radon transform A_μ exact inversion formulae exist [32, 36, 50]. In [32, 36] the unknown quantity f is required to be 'sufficiently smooth' (e.g. continuously differentiable f with compact support in [32]), in [50] it is assumed that μ is constant in the support of f. However, in medical applications, neither the activity f nor the density μ will fulfill these conditions. Furthermore, due to the measurement process, the given data will be noisy and hence, also

for the linear attenuated Radon transform regularization methods have to be used [19, 28].

We want to remark that although today's SPECT/CT imaging procedure is based on joint measurements, the reconstruction is still split into two steps. First, the density μ is reconstructed from the CT-data and second, the activity is reconstructed by plugging the reconstructed μ into the operator A and solving the linear equation $A_\mu f = z$, the so-called *attenuation correction* [14]. This has the disadvantage that the information about the density μ, which is contained in the SPECT-data, is not taken into account. Also, an inaccurate reconstruction of the density μ leads to the use of a wrong operator A_μ, which is yet another source for possibly bad reconstructions of f.

Also the problem of inverting (1.2) with μ unknown is considered in the literature: In [27, 34, 53] it is assumed that μ is a variation of a known prototype density distribution, e.g., an affine distortion of a known density μ_0. Methods for approximating both functions f and μ from SPECT data alone without a prototype density μ can be found in [16, 41, 42].

In the approach presented here we assume that we have two sets of data from an integrated SPECT/CT device available. But instead of first reconstructing the density μ and then using it to reconstruct the activity f from the linear attenuated Radon problem we achieve a simultaneous reconstruction of both f and μ by minimizing the functional

$$\|A(f,\mu) - y^\delta\|^2_{L^2(\mathbb{R}\times S^1)} \;+\; \beta\|R\mu - z^\delta\|^2_{L^2(\mathbb{R}\times S^1)} + \mathcal{P}(f,\mu)\ . \tag{1.3}$$

The functional consists of the weighted sum of two discrepancy terms, one for the SPECT data set y (in the case of noise y^δ) and one for the CT data set z (z^δ), and a penalty term $\mathcal{P}(f,\mu)$ which will be specified soon. The unknown distributions and the given data are connected via the Radon and the attenuated Radon transform. When minimizing the functional (1.3), the first two terms assure that the reconstructions of f and μ are 'close' (the meaning of closeness depends on the amount of noise, the penalty $\mathcal{P}$ and the weights β and α) to the solutions of the equations $A(f,\mu) = y$ and $R\mu = z$.

The penalty term $\mathcal{P}$ in (1.3) will be chosen to take into account that in many practical applications one is not only interested in the reconstructions of the density and/or activity distribution but also in the extraction of some specific features within the reconstructions. For example, the planning of surgery might require the determination of boundaries of inner organs like liver or lung, the separation of cancerous and healthy tissue and exact information about the blood flow or disturbances in the blood circulation like in the presence of coronary artery disease. In computerized tomography, the procedure for this usually includes first a reconstruction and – as a second step – a segmentation of the reconstructed images:

$$\text{data} \longrightarrow \text{reconstruction} \longrightarrow \text{segmentation}.$$

A segmentation of an image can be achieved by local criteria which attempt to classify image pixels according to their membership to certain regions, e.g., region growing algorithms [30]. Besides that also deformable interfaces (active contours, snakes, level-set methods) have been used for image segmentation: a collection of curves (or surfaces for higher dimensional data) is

introduced and updated such that the curves separate approximately homogeneous regions. For this, an energy functional is used which penalizes inhomogenities within the distinct regions and which is minimized with respect to the separating contours. Different energy functionals habe been considered: elastic energy in connection with edge detectors [6, 13, 22, 26], region based functionals [24, 25, 39] or Mumford-Shah like functionals [8, 10, 21]. Also for the description of the segmenting curves different geometric models have been used: parametrized snakes [49] or level-set techniques [37, 46]. For more details on this subject we refer to the monographs [1, 45].

The main drawback of the approach of first reconstructing and then segmenting is that the measured data are only used for the reconstruction of the (density or activity) distribution, but not for the segmentation. As the quality of the reconstructions is limited due to data noise an image postprocessing [52] might be necessary before segmentation:

$$\text{data} \longrightarrow \text{reconstruction} \longrightarrow \text{image postprocessing} \longrightarrow \text{segmentation}.$$

Hence, errors in the reconstruction (due to numerical problems, a wrong choice of regularization parameters or a wrong operator A_μ) will tamper the image postprocessing and by that also the segmentation.

The main goal of this paper is to achieve a simultaneous reconstruction and segmentation for the SPECT/CT problem *directly* from the data. It is a generalization of the ideas developed in [43] where the authors dealt with the linear CT problem. We introduce an algorithm that uses both data sets z^δ and y^δ, from CT and SPECT, and achieves simultaneously reconstructions of both f and μ as well as segmentations (Γ^f, Γ^μ) of (f, μ). For this, we consider the Mumford-Shah like functional

$$J(f,\mu,\Gamma^f,\Gamma^\mu) = \|A(f,\mu)-y^\delta\|^2_{L^2(\mathbb{R}\times S^1)}+\beta\|R\mu-z^\delta\|^2_{L^2(\mathbb{R}\times S^1)}+\alpha(|\Gamma^f|+|\Gamma^\mu|)\,, \tag{1.4}$$

i.e., we specify the penalty $\mathcal{P}$ in (1.3) to be a multiple of the length of the segmenting contours Γ^f and Γ^μ. The Mumford-Shah functional was originally designed to identify the set of singularities of a given function (e.g. a picture) and – simultaneously – to find a smooth approximation of the function away from the singularities [7, 10, 21, 31]. The classical Mumford-Shah functional for image segmentation has the form

$$J_{\mathrm{MS}}(y,\Gamma) = \|y-y^\delta\|^2 + \gamma\int_{D\setminus\Gamma}|\nabla y|^2dx + \beta|\Gamma|\ .$$

The MS-like functional (1.4) almost reduces to the classical MS-functional if we set $\beta = 0$ and replace $A(f,\mu)$ by the identity operator acting on the data y, the minimization is then done with respect to (y,Γ) instead of $(f,\mu,\Gamma_f,\Gamma_\mu)$. The first penalty in the classical Mumford-Shah functional, namely $\int_{D\setminus\Gamma}|\nabla y|^2dx$, assures that the approximation is smooth away from the singularity set Γ. For medical applications it is reasonable to restrict the reconstructions to activities f and densities μ which are constant with respect to a partition of the body, as the tissues of inner organs, bones, muscles have approximately constant density. In (1.4) the minimization is done over the restricted class of piecewise constant fuctions (and not piecewise smooth functions as in the case of the classical Mumford-Shah approach).

For piecewise constant functions, the penalty on the gradient of the reconstruction vanishes. The piecewise constant variant of the Mumford-Shah approach is sometimes called Chan-Vese approach [12]. When minimizing the Mumford-Shah like functional (1.4) the first two terms on the right hand side assure that the reconstructions fit the given data whereas the penalty term $(|\Gamma^f| + |\Gamma^\mu|)$ controls the length of the boundaries of the partitions of the images.

As discussed in [43], the main difficulty in using a Mumford-Shah like approach lies in the different structure of the geometric variable (the singularity set) and the functional variable (the reconstruction) which cannot be treated easily in a unified way within the framework of nonlinear optimization. To overcome this difficulty we proceed as follows: first, we fix the geometric variable and minimize the functional with respect to f and μ, see (2.4a). Second, we fix the functional variable and minimize the functional with respect to the geometry (Γ^f, Γ^μ), see (2.4b), which reduces the problem to a shape optimization problem [9, 21, 43, 51]. The update of the geometry is done using the level-set methodology. The combination of level-set and shape sensitivity techniques was first applied to inverse problems in [44], other level-set based methods for inverse problems involving shapes can be found in [2, 5, 11, 17, 18, 20, 23, 29, 38].

2. A piecewise constant Mumford-Shah functional for SPECT

2.1. **Problem setting.** Suppose we are given noisy data $y^\delta : \mathbb{R} \times S^1 \to \mathbb{R}$ of the attenuated Radon transform of unknown density $\mu : \mathbb{R}^2 \to \mathbb{R}$ and activity $f : \mathbb{R}^2 \to \mathbb{R}$ functions, i.e.

$$y^\delta(s,\omega) \sim A(f,\mu) = \int_{t\in\mathbb{R}} f(s\omega + t\omega^\perp)\, \exp\Big(- \int_{\tau=t}^{\infty} \mu(s\omega + \tau\omega^\perp)\, d\tau \Big)\, dt.$$

Simultaneously we (may) have measured data of the Radon transform of the density μ:

$$z^\delta(s,\omega) \sim R\mu = \int_{\mathbb{R}} \mu(s\omega + t\omega^\perp)\, dt.$$

Both functions μ and f are supposed to vanish outside a bounded domain $D \subset \mathbb{R}^2$. Moreover, we assume that both unknowns are piecewise constant with respect to (not-identical) partitions of the image domain $\mathbb{R}^2$. We explain what we mean by that for the case of the density function μ. Let us assume that there exists a finite collection of closed bounded curves $\Gamma^\mu \subset \mathbb{R}^2$ which are pairwise disjoint. The function values of μ are supposed to be constant on every connected component of Γ^μ. The assumption that μ has compact support immediately implies that $\mu = 0$ on the unbounded component of $\mathbb{R}^2 \setminus \Gamma^\mu$. To represent the bounding curves Γ^μ we use level-set techniques, i.e., we assume that $\Gamma^\mu = \{\mathbf{x} \in D : \phi^\mu(\mathbf{x}) = 0\}$ with a level set function $\phi^\mu : D \to \mathbb{R}$. The choice of level-sets for the description of Γ^μ automatically renders certain topological configurations (triple junctions, crossing branches) as unfeasible or at least as very singular. The (finitely many) bounded connected components of $\mathbb{R}^2 \setminus \Gamma^\mu$ are denoted by $\{\Omega_i^\mu\}_{i=1}^{n(\Gamma^\mu)}$ with $n(\Gamma^\mu) \in \mathbb{N}$ standing for the number of connected components of $\mathbb{R}^2 \setminus \Gamma^\mu$, not

counting the unbounded component. We make the same kind of assumptions for the activity function f. However, we allow the two functions μ and f to have different boundary curves Γ^μ and Γ^f respectively, and hence different partitions $\{\Omega_i^\mu\}_{i=1}^{n(\Gamma^\mu)}$ and $\{\Omega_j^f\}_{j=1}^{n(\Gamma^f)}$ of sets with constant function values.

Let Γ be any finite collection of pairwise disjoint, closed, bounded curves and let $\{\Omega_i^\Gamma\}_{i=1}^{n(\Gamma)}$ denote the set of all bounded connected components of $\mathbb{R}^2 \setminus \Gamma$. We define the space of piecewise constant functions with respect to the geometry Γ as

$$PC(\mathbb{R}^2 \setminus \Gamma) = \Big\{ \sum_{i=1}^{n(\Gamma)} \alpha_i \, \chi_{\Omega_i^\Gamma} \, : \, \alpha_i \in \mathbb{R} \Big\} \tag{2.1}$$

where χ_Ω denotes the characteristic function of the set Ω. The characteristic functions $\{\chi_{\Omega_i^\Gamma}\}_{i=1}^{n(\Gamma)}$ form a basis in $PC(\mathbb{R}^2 \setminus \Gamma)$. Note that the characteristic function of the unbounded component of $\mathbb{R}^2 \setminus \Gamma$ is not an element of the basis. To simplify notations we define $PC(\Gamma) := PC(\mathbb{R}^2 \setminus \Gamma)$.

We formulate the objective of the reconstruction problem as to find simultaneously the singularity sets Γ^f, Γ^μ and the functions $f \in PC(\Gamma^f)$, and $\mu \in PC(\Gamma^\mu)$ such that the given data y^δ and z^δ are fitted best possible in a least-squares sense. We therefore consider the Mumford-Shah like functional

$$J(f, \mu, \Gamma^f, \Gamma^\mu) = \|A(f,\mu) - y^\delta\|^2_{L^2(\mathbb{R}\times S^1)} + \beta \|R\mu - z^\delta\|^2_{L^2(\mathbb{R}\times S^1)} + \alpha(|\Gamma^f| + |\Gamma^\mu|), \tag{2.2}$$

where $|\Gamma^f|$ is the 1-dimensional Hausdorff measure of Γ^f (and analogously for $|\Gamma^\mu|$). Note that it is not necessary to add a regularization term for f since — for fixed Γ^f — the activity f is an element in the finite (usually low) dimensional space $PC(\Gamma^f)$. It follows that the identification of f from the data for fixed Γ^f is well-posed. However, the dependence of the functional on the geometric variable Γ^f might be sensitive. For this reason, the length term $\alpha|\Gamma^f|$ is added as a regularization term in the cost functional to guarantee well-posedness of the minimization of J with respect to the geometric variable. The same considerations hold for the density function μ and the corresponding singularity set Γ^μ.

2.2. **The reduced functional.** We introduce the compact notation

$$\Gamma = (\Gamma^f, \Gamma^\mu) \quad \text{and} \quad \zeta = (f, \mu) \in PC(\Gamma^f) \times PC(\Gamma^\mu) =: PC(\Gamma) \tag{2.3}$$

for a pair of feasible geometries and a corresponding pair of activity/density functions; the Mumford-Shah like functional (2.2) becomes $J = J(\zeta, \Gamma)$.

An algorithm for the minimization of the functional $J(\zeta, \Gamma)$ which updates both variables Γ and ζ independently is difficult to formulate. This is mainly due to the fact that the geometry Γ defines the domain of definition for the functional variable ζ and thus does not allow to treat ζ and Γ as independent. We therefore choose the following *reduced formulation*: For fixed Γ solve the variational problem

$$\min_{\zeta \in PC(\Gamma)} J(\zeta, \Gamma). \tag{2.4a}$$

Denote the solution by $\zeta(\Gamma)$. With that solve the *shape optimization problem*

$$\min_{\Gamma} \hat{J}(\Gamma) \text{ with } \hat{J}(\Gamma) = J(\zeta(\Gamma), \Gamma). \tag{2.4b}$$

The following section deals with the numerical treatment of the reduced formulation (2.4).

3. Minimization Algorithm

We now describe first in overview and later in detail the proposed numerical approach for the minimization of the reduced functional (2.4).

Step 1: Choose an initial estimate $\Gamma_0 = (\Gamma_0^f, \Gamma_0^\mu)$ for the geometries.
Step 2: For fixed Γ minimize J with respect to the pair $\zeta = (f, \mu) \in PC(\Gamma)$ by solving the respective optimality system. Denote the solution by $\zeta(\Gamma) = (f(\Gamma), \mu(\Gamma))$.
Step 3: Consider the reduced functional

$$\hat{J}(\Gamma) = J(\zeta(\Gamma), \Gamma). \tag{3.1}$$

Find a descent direction for the functional $\hat{J}$ with respect to the geometric variable Γ.
Step 4: Update Γ by moving it in the chosen descent direction according to an appropriate line-search rule. Use a level-set formulation for the update of the geometry.
Step 5: Check for optimality:
- If the shape gradient is large go to step 2.
- If the shape gradient is small determine the derivative of the cost functional with respect to the functional variable ζ. If a significant maximum or minimum exists for the functional gradient introduce a new component of Γ in the vicinity of the extremum. Go back to step 2.
- If none of the above holds: terminate the algorithm.

We now present a detailed description of the individual steps of the algorithm.

3.1. Step 2: Solution of the optimality system with respect to f and μ.

For fixed geometric variables $\Gamma = (\Gamma^f, \Gamma^\mu)$ we solve the variational problem

$$\min_{\substack{f \in PC(\Gamma^f) \\ \mu \in PC(\Gamma^\mu)}} \|A(f,\mu) - y^\delta\|^2_{L^2(\mathbb{R}\times S^1)} + \beta \|R\mu - z^\delta\|^2_{L^2(\mathbb{R}\times S^1)}. \tag{3.2}$$

3.1.1. *Optimality system.* The following proposition characterizes the solution to problem (3.2).

Proposition 1. *Assume that*

$$f(\mathbf{x}) = \sum_{i=1}^{n(\Gamma^f)} f_i \, \chi_{\Omega_i^f}(\mathbf{x}) \quad \textit{and} \quad \mu(\mathbf{x}) = \sum_{k=1}^{n(\Gamma^\mu)} \mu_k \, \chi_{\Omega_k^\mu}(\mathbf{x}) \tag{3.3}$$

is the solution to (3.2)*. The corresponding vectors of coefficients are denoted by* $\mathbf{f} = (f_i)_{i=1}^{n(\Gamma^f)}$ *and* $\boldsymbol{\mu} = (\mu_k)_{k=1}^{n(\Gamma^\mu)}$*. Then* $\mathbf{f}$ *and* $\boldsymbol{\mu}$ *solve the system of nonlinear equations in* $\mathbb{R}^{n(\Gamma^f)} \times \mathbb{R}^{n(\Gamma^\mu)}$*:*

$$M(\boldsymbol{\mu})\mathbf{f} = \mathbf{r}(\boldsymbol{\mu}) \tag{3.4a}$$

$$\mathbf{F}(\mathbf{f}, \boldsymbol{\mu}) + \beta \tilde{M}\, \boldsymbol{\mu} = \tilde{\mathbf{r}}_\beta(\mathbf{f}, \boldsymbol{\mu}) \tag{3.4b}$$

with

$$M = \big(m_{i,j}\big)_{i,j=1}^{n(\Gamma^f)}, \quad \mathbf{r} = \big(r_i\big)_{i=1}^{n(\Gamma^f)}, \tag{3.5}$$

$$\mathbf{F} = (F_k)_{k=1}^{n(\Gamma^\mu)}, \quad \tilde{M} = (\tilde{m}_{k,l})_{k,l=1}^{n(\Gamma^\mu)}, \quad \tilde{\mathbf{r}}_\beta = (\tilde{r}_k)_{k=1}^{n(\Gamma^\mu)}. \tag{3.6}$$

The terms in (3.5) *are*

$$m_{i,j} = \langle A(\chi_{\Omega_j^f}, \mu), A(\chi_{\Omega_i^f}, \mu)\rangle_{L_2(\mathbb{R}\times S^1)}$$

and

$$r_i = \langle y^\delta, A(\chi_{\Omega_i^f}, \mu)\rangle_{L_2(\mathbb{R}\times S^1)}\ . \tag{3.7a}$$

The terms in (3.6) *are*

$$F_k = \big\langle A(f,\mu), A'_f(\mu)\,\chi_{\Omega_k^\mu}\big\rangle_{L_2(\mathbb{R}\times S^1)}\ , \tag{3.7b}$$

$$\tilde{m}_{k,l} = \big\langle R\chi_{\Omega_l^\mu}, R\,\chi_{\Omega_k^\mu}\big\rangle_{L_2(\mathbb{R}\times S^1)} \tag{3.7c}$$

and

$$\tilde{r}_k = \big\langle y^\delta, A'_f(\mu)\,\chi_{\Omega_k^\mu}\big\rangle + \beta\big\langle z^\delta, R\,\chi_{\Omega_k^\mu}\big\rangle \tag{3.7d}$$

where $A'_f(\mu)$ *denotes the (partial) Fréchet derivative of the operator* A *with respect to the second variable for fixed* f*, see Lemma 1.*

Lemma 1. *For fixed* f *the (partial) Fréchet derivative of the operator* $A(f,\cdot)$ *with respect to the second variable is*

$$\big(A'_f(\mu)\,\nu\big)(s,\omega) =$$
$$-\int_{\sigma\in\mathbb{R}} \nu(s\omega+\sigma\omega^\perp) \int_{t=-\infty}^{\sigma} f(s\omega+t\omega^\perp)\, \exp\Big(-\int_{\tau=t}^{\infty} \mu(s\omega+\tau\omega^\perp)\,d\tau\Big)\,dt\,d\sigma.$$

for all $\nu \in L^2(\mathbb{R}^2)$*.*

For the proof of Lemma 1 see Proposition 3 from the appendix.

Proof of Proposition1. The Euler-Lagrange equations for (3.2) are

$$\frac{\partial J}{\partial f}\cdot \delta f = 0, \qquad \frac{\partial J}{\partial \mu}\cdot \delta\mu = 0 \tag{3.8}$$

for all admissible variations δf of f and $\delta\mu$ of μ. Since the characteristic functions

$$\{\chi_{\Omega_i^f}\}_{i=1}^{n(\Gamma^f)} \quad \text{and} \quad \{\chi_{\Omega_k^\mu}\}_{k=1}^{n(\Gamma^\mu)}$$

form bases in $PC(\Gamma^f)$ and $PC(\Gamma^\mu)$ respectively, it is sufficient to consider (3.8) for $\delta f = \chi_{\Omega_i^f}$ and $\delta\mu = \chi_{\Omega_k^\mu}$. The first Euler-Lagrange equation in (3.8) then reads as

$$\langle A(f,\mu) - y^\delta, A(\chi_{\Omega_i^f}, \mu)\rangle_{L^2(\mathbb{R}\times S^1)} = 0 \tag{3.9}$$

for all $i = 1, \dots, n(\Gamma^f)$. Since the operator A acts linearly on f (and hence on $\mathbf{f}$), the optimality condition (3.9) can be written as a finite dimensional linear system

$$M(\boldsymbol{\mu})\mathbf{f} = \mathbf{r} \tag{3.10}$$

for the vector of unknown coefficients $\mathbf{f}$. The matrix M is given as

$$M = \big(m_{i,j}\big)_{i,j=1}^{n(\Gamma^f)} \quad \text{with} \quad m_{i,j} = \langle A(\chi_{\Omega_j^f}, \mu), A(\chi_{\Omega_i^f}, \mu)\rangle_{L^2(\mathbb{R}\times S^1)} \tag{3.11}$$

and thus (3.7a) holds. The right-hand side of (3.10) is

$$\mathbf{r} = \big(r_i\big)_{i=1}^{n(\Gamma^f)} \text{ with } r_i = \langle y^\delta, A(\chi_{\Omega_i^f}, \mu)\rangle_{L^2(\mathbb{R}\times S^1)} \tag{3.12}$$

which proves (3.7a).

We continue with the investigation of the second Euler-Lagrange equation in (3.8). Taking test-functions in the basis $\{\chi_{\Omega_k^\mu}\}_{k=1}^{n(\Gamma^\mu)}$ we obtain

$$\big\langle A(f,\mu) - y^\delta, A_f'(\mu)\,\chi_{\Omega_k^\mu}\big\rangle + \beta\big\langle R\mu - z^\delta, R\,\chi_{\Omega_k^\mu}\big\rangle = 0 \tag{3.13}$$

for all $k = 1, \dots, n(\Gamma^\mu)$. Acting on the coefficient vectors $\mathbf{f}$ and $\boldsymbol{\mu}$, the optimality condition (3.13) has the form of the non-linear equation

$$\mathbf{F}(\mathbf{f}, \boldsymbol{\mu}) + \beta\tilde{M}\,\boldsymbol{\mu} = \tilde{\mathbf{r}}_\beta(\mathbf{f}, \boldsymbol{\mu}). \tag{3.14}$$

Here $\mathbf{F} = (F_k)_{k=1}^{n(\Gamma^\mu)}$ with

$$F_k = \big\langle A(f,\mu), A_f'(\mu)\,\chi_{\Omega_k^\mu}\big\rangle, \tag{3.15}$$

and hence, (3.7b) holds. From (3.13) and (3.14) we conclude that $\tilde{M} = (\tilde{m}_{k,l})_{k,l=1}^{n(\Gamma^\mu)}$ with

$$\tilde{m}_{k,l} = \big\langle R\chi_{\Omega_l^\mu}, R\,\chi_{\Omega_k^\mu}\big\rangle \tag{3.16}$$

and hence (3.7c). The right-hand side of (3.14) is given as $\tilde{\mathbf{r}}_\beta = (\tilde{r}_k)_{k=1}^{n(\Gamma^\mu)}$ with

$$\tilde{r}_k = \big\langle y^\delta, A_f'(\mu)\,\chi_{\Omega_k^\mu}\big\rangle + \beta\big\langle z^\delta, R\,\chi_{\Omega_k^\mu}\big\rangle \tag{3.17}$$

which shows (3.7d) and concludes the proof. □

3.1.2. *Solution method for the optimality system* (3.4). The nonlinear optimality system (3.4) is solved with the standard Newton method. We consider the equivalent problem of finding zeros of

$$\begin{aligned}\mathbf{g_1} &:= \mathbf{g_1}(\mathbf{f}, \boldsymbol{\mu}) = M(\boldsymbol{\mu})\mathbf{f} - \mathbf{r}(\boldsymbol{\mu})\\ \mathbf{g_2} &:= \mathbf{g_2}(\mathbf{f}, \boldsymbol{\mu}) = \mathbf{F}(\mathbf{f}, \boldsymbol{\mu}) + \beta\tilde{M}\,\boldsymbol{\mu} - \tilde{\mathbf{r}}_\beta(\mathbf{f}, \boldsymbol{\mu})\ .\end{aligned}$$

Sequences of approximating solutions $(\mathbf{f}^{n+1}, \boldsymbol{\mu}^{n+1})$ are defined iteratively as $(\mathbf{f}^{n+1}, \boldsymbol{\mu}^{n+1}) := (\mathbf{f}^n, \boldsymbol{\mu}^n) + (\triangle\mathbf{f}, \triangle\boldsymbol{\mu})$. We use the shortcut $\mathbf{g_*}^n = \mathbf{g_*}(\mathbf{f}^n, \boldsymbol{\mu}^n)$. The correction $(\triangle\mathbf{f}, \triangle\boldsymbol{\mu})$ is found as solution to the linearized system

$$\begin{pmatrix} A & B \\ C & D \end{pmatrix} \cdot \begin{pmatrix} \triangle\mathbf{f} \\ \triangle\boldsymbol{\mu} \end{pmatrix} = \begin{pmatrix} \partial_{\mathbf{f}^n}\mathbf{g_1}^n & \partial_{\boldsymbol{\mu}^n}\mathbf{g_1}^n \\ \partial_{\mathbf{f}^n}\mathbf{g_2}^n & \partial_{\boldsymbol{\mu}^n}\mathbf{g_2}^n \end{pmatrix} \cdot \begin{pmatrix} \triangle\mathbf{f} \\ \triangle\boldsymbol{\mu} \end{pmatrix} = - \begin{pmatrix} \mathbf{g_1}^n \\ \mathbf{g_2}^n \end{pmatrix}\ . \tag{3.18}$$

To simplify notation, the upper index is supressed in the following. The entries of the right hand side of (3.18) are

$$\begin{aligned}
\mathbf{g_1}_i &= (M(\boldsymbol{\mu})\mathbf{f} - \mathbf{r}(\boldsymbol{\mu}))_i = \sum_{j=1}^{n(\Gamma^f)} m_{ij} f_j - r_i \\
&\overset{(3.7a),(3.7a)}{=} \langle A(f,\mu) - y^\delta, A(\chi_{\Omega_i^f},\mu)\rangle \qquad i = 1,\dots,n(\Gamma^f)\ , \\
\mathbf{g_2}_i &= \Big(\mathbf{F}(\mathbf{f},\boldsymbol{\mu}) + \beta\tilde{M}\,\boldsymbol{\mu} - \tilde{\mathbf{r}}_\beta(\mathbf{f},\boldsymbol{\mu})\Big)_i = (\mathbf{F}(\mathbf{f},\boldsymbol{\mu}) - \tilde{\mathbf{r}}_\beta(\mathbf{f},\boldsymbol{\mu}))_i + (\beta\tilde{M}\,\boldsymbol{\mu})_i \\
&\overset{(3.15),(3.17)}{=} \langle A(f,\mu) - y^\delta, A'_f(\mu)\chi_{\Omega_i^\mu}\rangle - \beta\langle z^\delta, R\chi_{\Omega_i^\mu}\rangle + \beta\sum_{j=1}^{n(\Gamma^\mu)} \tilde{m}_{ij}\mu_j \\
&\overset{(3.16)}{=} \langle A(f,\mu) - y^\delta, A'_f(\mu)\chi_{\Omega_i^\mu}\rangle + \beta\langle R\mu - z^\delta, R\chi_{\Omega_i^\mu}\rangle \qquad i = 1,\dots,n(\Gamma^\mu)\ .
\end{aligned}$$

The entries of the four-block Newton matrix of (3.18) are

$$\begin{aligned}
A_{ij} &= (\partial_{\mathbf{f}}\mathbf{g_1})_{ij} = (\partial_{\mathbf{f}} M(\boldsymbol{\mu})\mathbf{f})_{ij} = (M(\boldsymbol{\mu}))_{ij} = m_{ij} \\
&\overset{(3.7a)}{=} \langle A(\chi_{\Omega_j^f},\mu), A(\chi_{\Omega_i^f},\mu)\rangle \qquad i,j = 1,\dots,n(\Gamma^f)\ , \\
B_{ij} &= (\partial_{\boldsymbol{\mu}}\mathbf{g_1})_{ij} = (\partial_{\boldsymbol{\mu}}(M(\boldsymbol{\mu})\mathbf{f} - \mathbf{r}(\boldsymbol{\mu})))_{ij} = \partial_{\mu_j}\mathbf{g_1}_i \\
&= \langle A'_f(\mu)\chi_{\Omega_j^\mu}, A(\chi_{\Omega_i^f},\mu)\rangle + \langle A(f,\mu) - y^\delta, A'_{\chi_{\Omega_i^f}}(\mu)\chi_{\Omega_j^\mu}\rangle \\
&\qquad i = 1,\dots,n(\Gamma^f), j = 1,\dots,n(\Gamma^\mu)\ , \\
C_{ij} &= (\partial_{\mathbf{f}}\mathbf{g_2})_{ij} = \partial_{f_j}\mathbf{g_2}_i = \partial_{f_j}\langle A(f,\mu) - y^\delta, A'_f(\mu)\chi_{\Omega_i^\mu}\rangle \\
&= \langle A(\chi_{\Omega_j^f},\mu), A'_f(\mu)\chi_{\Omega_i^\mu}\rangle + \langle A(f,\mu) - y^\delta, A'_{\chi_{\Omega_i^f}}(\mu)\chi_{\Omega_i^\mu}\rangle = B_{ji}\ .
\end{aligned}$$

For the last part of the Newton matrix in (3.18) we need to compute a second derivative of $A(f,\mu)$ with respect to the second variable, see Lemma 2. It is

$$\begin{aligned}
D_{ij} &= (\partial_{\boldsymbol{\mu}}\mathbf{g_2})_{ij} = \partial_{\boldsymbol{\mu}_j}\mathbf{g_2}_i \\
&= \partial_{\boldsymbol{\mu}_j}\Big[\langle A(f,\mu) - y^\delta, A'_f(\mu)\chi_{\Omega_i^\mu}\rangle + \beta\langle R\mu - z^\delta, R\chi_{\Omega_i^\mu}\rangle\Big] \\
&= \langle A'_f(\mu)\chi_{\Omega_j^\mu}, A'_f(\mu)\chi_{\Omega_i^\mu}\rangle + \beta\langle R\chi_{\Omega_j^\mu}, R\chi_{\Omega_i^\mu}\rangle \\
&\quad + \langle A(f,\mu) - y^\delta, A''_f(\mu)(\chi_{\Omega_i^\mu}, \chi_{\Omega_j^\mu})\rangle \qquad i,j = 1,\dots,n(\Gamma^\mu)\ .
\end{aligned}$$

Lemma 2. *The linearization of $A'_f(\mu)\nu$ with respect to μ is given as*

$$\begin{aligned}
A''_f(\mu)(\nu,h) = \int_{t\in\mathbb{R}} & f(s\omega + t\omega^\perp)\exp\big(-\textstyle\int_{\tau=t}^\infty \mu(s\omega+\tau\omega^\perp)d\tau\big) \\
& \cdot \big(\textstyle\int_{\tau=t}^\infty h(s\omega+\tau\omega^\perp)d\tau\big)\big(\textstyle\int_{\tau=t}^\infty \nu(s\omega+\tau\omega^\perp)d\tau\big)\ dt\ .
\end{aligned}$$

Proof. It is (compare (A.4) from the appendix)

$$\begin{aligned}
A'_f(\mu+h)\nu = -\int_{t\in\mathbb{R}} & f(s\omega + t\omega^\perp)\exp\big(-\textstyle\int_{\tau=t}^\infty (\mu+h)(s\omega+\tau\omega^\perp)d\tau\big) \\
& \cdot \big(\textstyle\int_{\tau=t}^\infty \nu(s\omega+\tau\omega^\perp)d\tau\big)\ dt\ .
\end{aligned}$$

With $\exp(A(\mu+h)) = \exp(A\mu) + Ah\exp(A\mu) + \mathcal{O}(\|h\|^2)$ it is

$$\begin{aligned} A'_f(\mu+h)\nu = &- \int_{t\in\mathbb{R}} f(s\omega+t\omega^\perp)\exp\big(-\textstyle\int_{\tau=t}^{\infty}\mu(s\omega+\tau\omega^\perp)d\tau\big) \\ &\cdot\big(\textstyle\int_{\tau=t}^{\infty}\nu(s\omega+\tau\omega^\perp)d\tau\big)\ dt \\ &+ \int_{t\in\mathbb{R}} f(s\omega+t\omega^\perp)\exp\big(-\textstyle\int_{\tau=t}^{\infty}\mu(s\omega+\tau\omega^\perp)d\tau\big) \\ &\cdot\big(\textstyle\int_{\tau=t}^{\infty}h(s\omega+\tau\omega^\perp)d\tau\big)\big(\textstyle\int_{\tau=t}^{\infty}\nu(s\omega+\tau\omega^\perp)d\tau\big)\ dt \\ &+ \mathcal{O}(\|h\|^2)\ . \end{aligned}$$

It follows

$$\begin{aligned} &A'_f(\mu+h)\nu - A'_f(\mu)\nu \\ &\quad= \int_{t\in\mathbb{R}} f(s\omega+t\omega^\perp)\exp\big(-\textstyle\int_{\tau=t}^{\infty}\mu(s\omega+\tau\omega^\perp)d\tau\big) \\ &\qquad\cdot\big(\textstyle\int_{\tau=t}^{\infty}h(s\omega+\tau\omega^\perp)d\tau\big)\big(\textstyle\int_{\tau=t}^{\infty}\nu(s\omega+\tau\omega^\perp)d\tau\big)\ dt \\ &\qquad+ \mathcal{O}(\|h\|^2)\ . \end{aligned}$$

□

3.2. **Step 3: Shape sensitivity analysis of the reduced functional and choice of the descent direction.** We make some assumptions on the nature of the perturbations of the shape variables Ω^f and Ω^μ. Using the level-set representation ϕ^μ for the geometry Γ^μ we define the update of a geometry Γ_0^μ in the level-set context as

$$\Gamma^\mu(t) = \{\mathbf{x}\in\mathbb{R}^2\ :\ \phi^\mu(\mathbf{x},t) = 0\}$$

where $\phi^\mu(\mathbf{x},t)$ is the solution to

$$\phi_t^\mu + F|\nabla\phi^\mu| = 0 \text{ and } \phi^\mu(\mathbf{x},0) = \phi_0^\mu$$

with $\Gamma_0^\mu = \{\phi_0^\mu = 0\}$. The scalar speed function F acts as the direction of perturbation for the update of the geometry. The connection of the scalar speed function with a speed vector field $\mathbf{v}$ which defines an (up to first order) equivalent perturbation of the geometry is given by

$$F(\mathbf{x}) = \langle \mathbf{v}(\mathbf{x}), \nabla b_{\Gamma^\mu}(\mathbf{x})\rangle, \tag{3.19}$$

for $\mathbf{x}\in\Gamma^\mu$, where b_{Γ^μ} denotes the signed distance function of the interface Γ^μ. In shape sensitivity analysis, expressions of the form $\langle \mathbf{v}, \mathbf{n}_{\Omega_i^\mu}\rangle$ frequently occur. Here $\mathbf{n}_{\Omega_i^\mu}$ is the exterior unit normal vector field to the set Ω_i^μ. We set $s_i^\mu = -\text{sign}(\phi^\mu(\mathbf{z}))$ for some $\mathbf{z}\in\Omega_i^\mu$ for the sign of the component Ω_i^μ. With this, we have

$$\langle \mathbf{v}, \mathbf{n}_{\Omega_i^\mu}\rangle = s_i^\mu F \tag{3.20}$$

and we can express the directional derivative of a functional at the shape Γ^μ in terms of the level-set type speed function F. The analogous specifications shall hold for the shape variable Γ^f.

In the following we use some well-known results from shape sensitivity analysis. The differentiation rules for domain and boundary functionals of the form

$$J_d(\Omega) = \int_\Omega g d\mathbf{x} \quad \text{and} \quad J_b(\Gamma) = \int_\Gamma h dS$$

are given by

$$\begin{aligned} dJ_d(\Omega;F) &= s_\Omega \int_{\partial\Omega} g\,F\,dS \quad \text{and} \\ dJ_b(\Omega;F) &= \int_\Gamma (\langle \nabla h, \nabla b_{\Gamma^\mu}\rangle + f \triangle b_{\Gamma^\mu})\,F\,dS\,. \end{aligned} \tag{3.21}$$

Here $\triangle b_\Gamma = s_\Omega \cdot \kappa$ where κ is the mean curvature of Γ, see [15, 22, 48] for more details. In the following, we apply these rules to the reduced functional of the SPECT/CT problem, $\hat{J}(\Gamma) = \hat{J}\big((\Gamma^f, \Gamma^\mu)\big)$, given as

$$\begin{aligned} \hat{J}\big((\Gamma^f,\Gamma^\mu)\big) = \int_{s\in\mathbb{R}} \int_{\omega\in S^1} \Bigg[\int_{t\in\mathbb{R}} \sum_{i=1}^{n(\Gamma^f)} f_i\, \chi_{\Omega_i^f}(s\omega + t\omega^\perp) \\ \cdot \exp\Big(-\textstyle\int_{\tau=t}^{\infty} \sum_{k=1}^{n(\Gamma^\mu)} \mu_k\, \chi_{\Omega_k^\mu}(s\omega+\tau\omega^\perp)\,d\tau\Big)\,dt - y^\delta(s,\omega)\Bigg]^2 d\omega\,ds \\ + \beta \int_{s\in\mathbb{R}} \int_{\omega\in S^1} \Bigg[\int_{t\in\mathbb{R}} \sum_{k=1}^{n(\Gamma^\mu)} \mu_k\, \chi_{\Omega_k^\mu}(s\omega+t\omega^\perp)\,dt - z^\delta(s,\omega)\Bigg]^2 d\omega\,ds \\ + \alpha(|\Gamma^f| + |\Gamma^\mu|). \end{aligned} \tag{3.22}$$

The obvious geometry dependent terms which have to be considered in the shape derivative are, in the first three rows, the domains of the characteristic functions, i.e., Ω_i^f, Ω_k^μ, Ω_k^μ, and in the last row, the boundaries of the domains, i.e., Γ^f, Γ^μ (all marked in red in the online version). Also the vectors $\mathbf{f} = (f_i)_{i=1}^{n(\Gamma^f)}$ and $\boldsymbol{\mu} = (\mu_k)_{k=1}^{n(\Gamma^\mu)}$ are geometry dependent as they are found as solutions to the optimality system described in Proposition 1. Hence, this dependence must be dealt with in the subsequent shape sensitivity analysis. We shall see, however, that the contribution from the shape derivatives $\mathbf{f}'(\Gamma^f;F)$ and $\boldsymbol{\mu}'(\Gamma^\mu;G)$ vanish. The derivative of the reduced functional $\hat{J}(\Gamma) = J(\zeta(\Gamma),\Gamma)$ with respect to Γ formally reads as

$$d\hat{J}(\Gamma;F) = \partial_\zeta J(\zeta(\Gamma),\Gamma)\zeta'(\Gamma;F) + d_\Gamma J(\zeta(\Gamma),\Gamma;F)$$

where $\partial_\zeta J$ denotes the derivative with respect to ζ for fixed Γ, $\zeta'(\Gamma;F)$ is the shape derivative of ζ with respect to Γ in direction F and $d_\Gamma J(\zeta(\Gamma),\Gamma;F)$ denotes the Eulerian derivative of J in direction F for fixed ζ.

Recall that $\mathbf{f}$ was found as the solution to the optimality system (3.8). Written as a function of the coefficient vector $\mathbf{f}$ the first equation in (3.8) has the form

$$\big\langle \nabla_{\mathbf{f}} J\big(\mathbf{f},\boldsymbol{\mu},\Gamma^f,\Gamma^\mu\big), \tilde{\mathbf{f}}\big\rangle_{\mathbb{R}^{n(\Gamma^f)}} = 0 \tag{3.23}$$

for all vectors $\tilde{\mathbf{f}} \in \mathbb{R}^{n(\Gamma^f)}$. The shape derivative of $\mathbf{f}$ occurs in the shape derivative of the reduced cost functional (3.1) as an inner derivative in the expression

$$\big\langle \nabla_{\mathbf{f}} J\big(\mathbf{f},\boldsymbol{\mu},\Gamma^f,\Gamma^\mu\big), \mathbf{f}'(\Gamma^f;F)\big\rangle_{\mathbb{R}^{n(\Gamma^f)}}.$$

This inner product, however, vanishes due to (3.23). The same argument can be used to show that the shape derivative of the vector $\boldsymbol{\mu}$ does not occur in the shape derivative of the reduced functional.

For the penalty on the length of the perimeter, the rule (3.21) immediately applies. The shape derivatives $d_{\Gamma^f} J$ and $d_{\Gamma^\mu} J$ with respect to Γ^f and Γ^μ are computed in the following.

Lemma 3. *Let A_μ^* denote the adjoint of the attenuated Radon transform w.r.t. the first argument. The shape derivative $d_{\Gamma^f} J_A(\Gamma^f; F)$ in direction F of the functional*

$$\hat{J}_A(\Gamma^f) = \|A(f,\mu) - y^\delta\|^2_{L^2(\mathbb{R}\times S^1)} \quad \textit{with } f = f(\Gamma^f)$$

is given by

$$d_{\Gamma^f}\hat{J}_A(\Gamma^f; F) = 2\sum_{i=1}^{n(\Gamma^f)} s_i^f\, f_i \int_{\partial\Omega_i^f} A_\mu^*\big(A(f,\mu) - y^\delta\big)(\mathbf{x}) F(\mathbf{x}) dS(\mathbf{x}) \ . \quad (3.24)$$

Proof. It is

$$\frac{1}{2} d_{\Gamma^f}\hat{J}_A(\Gamma^f; F) = \big\langle A(f,\mu) - y^\delta, d_{\Gamma^f}\big(A(f,\mu); F\big)\big\rangle_{L^2(\mathbb{R}\times S^1)} \ .$$

We introduce the shortcut $g = A(f,\mu) - y^\delta$. Since $A(f,\mu)$ is linear in f and $f \in \mathrm{PC}_m$ it follows

$$\begin{aligned}\frac{1}{2} d_{\Gamma^f}\hat{J}_A(\Gamma^f; F) &= \sum_{i=1}^{n(\Gamma^f)} f_i \big\langle\, g,\, d_{\Gamma^f}\big(A(\chi_{\Omega_i^f},\mu); F\big)\big\rangle_{L^2(\mathbb{R}\times S^1)} \\ &= \sum_{i=1}^{n(\Gamma^f)} f_i \int_{s\in\mathbb{R}}\int_{\omega\in S^1} g(s,w) \\ &\quad d_{\Gamma^f}\left[\int_{t\in\mathbb{R}} \chi_{\Omega_i^f}(s\omega + t\omega^\perp) \exp\big(-\textstyle\int_{\tau=-t}^\infty \mu(s\omega+\tau\omega^\perp)d\tau\big); F\right] d\omega ds \ .\end{aligned}$$

We want to exchange the order of differentiation (i.e., the shape derivative d_{Γ^f}) and integration for the integration variable s. Doing so, we must ignore the shape dependence of the term $g = A(f,\mu) - y^\delta$ in the differentiation even though the term formally appears inside the action of the differential operator. With the transformation $\mathbf{x} = s\omega + t\omega^\perp$, i.e., $s = \langle \mathbf{x}, \omega\rangle$ and $t = \langle \mathbf{x}, \omega^\perp\rangle$ respectively, it is

$$\begin{aligned}\frac{1}{2} d_{\Gamma^f}\hat{J}_A(\Gamma^f; F) = \sum_{i=1}^{n(\Gamma^f)} f_i \int_{\omega\in S^1} d_{\Gamma^f}\Big[\int_{\mathbf{x}\in\Omega_i^f} g(\langle\mathbf{x},\omega\rangle,\omega) \\ \cdot \exp\big(-\textstyle\int_{\tau=\langle\mathbf{x},\omega^\perp\rangle}^\infty \mu\big(\langle\mathbf{x},\omega\rangle\,\omega + \tau\omega^\perp\big)\,d\tau\big)\,d\mathbf{x}; F\Big]\, d\omega \ .\end{aligned}$$

We now deal with the differentiation of a domain integral over Ω_i^f. Applying the corresponding rule (3.21), we get

$$\begin{aligned}\frac{1}{2} d_{\Gamma^f} \hat{J}_A(\Gamma^f; F) &= \sum_{i=1}^{n(\Gamma^f)} s_i^f \, f_i \int_{\mathbf{x}\in\partial\Omega_i^f} \int_{\omega\in S^1} g(\langle \mathbf{x}, \omega\rangle, \omega) \\ &\qquad \cdot \exp\big(- \textstyle\int_{\tau=0}^{\infty} \mu(\mathbf{x} + \tau\omega^{\perp}) \, d\tau\big) \, d\omega \; F \, dS(\mathbf{x}) \\ &= \sum_{i=1}^{n(\Gamma^f)} s_i^f \, f_i \int_{\mathbf{x}\in\partial\Omega_i^f} A_\mu^* g\,(\mathbf{x}) F(\mathbf{x}) dS(\mathbf{x}) \; .\end{aligned}$$

□

For the Radon transform an equivalent result holds.

Corollary 1. *Let R^* denote the adjoint of the Radon transform. The shape derivative $d_{\Gamma^\mu} \hat{J}_R(\Gamma^\mu; G)$ in direction G of the functional*

$$\hat{J}_R(\Gamma^\mu) = \|R\mu - z^\delta\|^2_{L^2(\mathbb{R}\times S^1)} \quad \textit{with } \mu = \mu(\Gamma^\mu)$$

is given by

$$d_{\Gamma^\mu} \hat{J}_R(\Gamma^\mu; G) = 2 \sum_{k=1}^{n(\Gamma^\mu)} s_k^\mu \, \mu_k \int_{\partial\Omega_k^\mu} R^*\big(R\mu - z^\delta\big)(\mathbf{x}) G(\mathbf{x}) dS(\mathbf{x}) \; . \tag{3.25}$$

The proof proceeds along similar lines as the proof of Lemma 3 and can be found in [43].

In Lemma 3 the attenuated Radon transform $A(f, \mu)$ was considered with respect to the linear variable f. The following result is on the (nonlinear) dependence on the variable μ.

Lemma 4. *Let $(A'_f(\mu))^*$ denote the adjoint of the Frechet derivative of the attenuated Radon transform w.r.t. the second argument (the concrete expression is given in the appendix A.3). The shape derivative $d_{\Gamma^\mu} \hat{J}_A(\Gamma^\mu; G)$ in direction G of the functional*

$$\hat{J}_A(\Gamma^\mu) = \|A(f, \mu) - y^\delta\|^2_{L^2(\mathbb{R}\times S^1)} \quad \textit{with } \mu = \mu(\Gamma^\mu)$$

is given by

$$d_{\Gamma^\mu} \hat{J}_A(\Gamma^\mu; G) = -2 \sum_{k=1}^{n(\Gamma^\mu)} s_k^\mu \, \mu_k \int_{\partial\Omega_k^\mu} \big((A'_f(\mu))^*(A(f, \mu) - y^\delta)\big)(\mathbf{x}) G(\mathbf{x}) dS(\mathbf{x}) \; . \tag{3.26}$$

Proof. It is

$$\begin{aligned}
\frac{1}{2} d_{\Gamma^\mu} J(\Gamma^\mu; G) &= \big\langle \underbrace{A(f,\mu) - y^\delta}_{=:g}, d_{\Gamma^\mu}\big(A(f,\mu); G\big)\big\rangle_{L^2(\mathbb{R}\times S^1)} \\
&= \int_{s\in\mathbb{R}} \int_{\omega\in S^1} g(s,\omega) \\
&\qquad d_{\Gamma^\mu}\left[\int_{t\in\mathbb{R}} f(s\omega + t\omega^\perp) \exp\big(-\textstyle\int_{\tau=t}^{\infty} \mu(s\omega+\tau\omega^\perp)d\tau\big)dt;\, G\right] d\omega ds \\
&= \int_{s\in\mathbb{R}} \int_{\omega\in S^1} g(s,\omega) \\
&\qquad \int_{t\in\mathbb{R}} f(s\omega + t\omega^\perp) \exp\big(-\textstyle\int_{\sigma=t}^{\infty} \mu(s\omega+\sigma\omega^\perp)d\sigma\big) \\
&\qquad\qquad d_{\Gamma^\mu}\left[-\int_{\tau=t}^{\infty} \sum_{k=1}^{n(\Gamma^\mu)} \mu_k \chi_{\Omega_k^\mu}(s\omega+\tau\omega^\perp)d\tau;\, G\right] dt\, d\omega\, ds
\end{aligned}$$

where we have used the chain rule twice. Keeping in mind that the differentiation w.r.t. the shape variable Γ^μ is only to be carried out for the Γ^μ-dependent terms in the last line, we exchange the order or differentiation and integration,

$$\begin{aligned}
\frac{1}{2} d_{\Gamma^\mu} \hat{J}_A(\Gamma^\mu; G) = -d_{\Gamma^\mu}\Big[&\sum_{k=1}^{n(\Gamma^\mu)} \mu_k \int_{s\in\mathbb{R}} \int_{\omega\in S^1} g(s,\omega) \\
&\int_{t\in\mathbb{R}} f(s\omega + t\omega^\perp) \exp\big(-\textstyle\int_{\sigma=t}^{\infty} \mu(s\omega+\sigma\omega^\perp)d\sigma\big) \\
&\int_{\tau=t}^{\infty} \chi_{\Omega_k^\mu}(s\omega+\tau\omega^\perp)d\tau\, dt\, d\omega\, ds;\, G\Big] \,.
\end{aligned}$$

Exchanging the order of integration for τ and t yields further

$$\begin{aligned}
\frac{1}{2} d_{\Gamma^\mu} \hat{J}_A(\Gamma^\mu; G) = -d_{\Gamma^\mu}\Big[&\sum_{k=1}^{n(\Gamma^\mu)} \mu_k \int_{s\in\mathbb{R}} \int_{\omega\in S^1} g(s,\omega) \\
&\int_{\tau=-\infty}^{\infty} \int_{t=-\infty}^{\tau} f(s\omega + t\omega^\perp) \exp\big(-\textstyle\int_{\sigma=t}^{\infty} \mu(s\omega+\sigma\omega^\perp)d\sigma\big) \\
&\chi_{\Omega_k^\mu}(s\omega+\tau\omega^\perp)dt\, d\tau\, d\omega\, ds;\, G\Big] \,.
\end{aligned}$$

Substituting $\mathbf{x} = s\omega + \tau\omega^\perp$, i.e., $s = \langle \mathbf{x}, \omega\rangle$ and $\tau = \langle \mathbf{x}, \omega^\perp\rangle$ transforms the two integrals over s and ω into one integral over $\mathbb{R}^2$. As $\chi_{\Omega_k^\mu}$ is part of the integrand it is a domain integral over Ω_k^μ and application of the

differentiation rule (3.21) completes the proof:

$$\begin{aligned}\frac{1}{2}d_{\Gamma^\mu}J(\Gamma^\mu;G) &= -d_{\Gamma^\mu}\Big[\sum_{k=1}^{n(\Gamma^\mu)}\mu_k\int_{\mathbf{x}\in\mathbb{R}^2}\chi_{\Omega_k^\mu}(\mathbf{x})\int_{\omega\in S^1}g(\langle x,\omega\rangle,\omega)\\ &\qquad\int_{t=-\infty}^{0}f(\mathbf{x}+t\omega^\perp)\exp\big(-\textstyle\int_{\sigma=t}^{\infty}\mu(\mathbf{x}+\sigma\omega^\perp)d\sigma\big)dt\,d\omega\,d\mathbf{x};G\Big]\\ &= -d_{\Gamma^\mu}\Big[\sum_{k=1}^{n(\Gamma^\mu)}\mu_k\int_{\mathbf{x}\in\Omega_k^\mu}\big((A_f'(\mu))^*g\big)(\mathbf{x})d\mathbf{x}\,;G\Big]\\ &= -\sum_{k=1}^{n(\Gamma^\mu)}s_k^\mu\,\mu_k\int_{\mathbf{x}\in\partial\Omega_k^\mu}\big((A_f'(\mu))^*g\big)(\mathbf{x})G(\mathbf{x})\,dS(\mathbf{x})\ .\end{aligned}$$

□

Proposition 2. *For fixed μ let A_μ^* denote the adjoint of the attenuated Radon transform w.r.t. the argument f (see* (A.1)*). For fixed f let $(A_f'(\mu))^*$ denote the adjoint of the Frechet derivative of the attenuated Radon transform A w.r.t. the argument μ (see* (A.3)*).*

With $g = A(f,\mu) - y^\delta$ and $h = R\mu - z^\delta$, the shape derivatives w.r.t. Γ^f and Γ^μ of the reduced funtional $\hat{J}(\Gamma) = \hat{J}\big((\Gamma^f,\Gamma^\mu)\big)$, see (3.22)*, are given as*

$$\begin{aligned}d_{\Gamma^f}\hat{J}(\Gamma^f;F) &= 2\sum_{i=1}^{n(\Gamma^f)}s_i^f\,f_i\int_{\mathbf{x}\in\partial\Omega_i^f}A_\mu^*g(\mathbf{x})\,F\,dS\\ &\quad+\ \alpha\int_{\Gamma^f}\triangle b_{\Gamma^f}\,F\,dS\ ,\end{aligned}\tag{3.27}$$

$$\begin{aligned}d_{\Gamma^\mu}\hat{J}(\Gamma^\mu;G) &= -2\sum_{k=1}^{n(\Gamma^\mu)}s_k^\mu\,\mu_k\int_{\mathbf{x}\in\partial\Omega_k^\mu}\big[((A_f'(\mu))^*g)(\mathbf{x}) - \beta\,R^*h(\mathbf{x})\big]\,G\,dS\\ &\quad+\ \alpha\int_{\Gamma^\mu}\triangle b_{\Gamma^\mu}\,G\,dS\ .\end{aligned}\tag{3.28}$$

Proof. For the shape derivative w.r.t. Γ^f we have to compute

$$d_{\Gamma^f}\Big[\|A(f(\Gamma^f),\mu) - y^\delta\|^2_{L^2(\mathbb{R}\times S^1)} + \alpha|\Gamma^f|\,;\ F\Big]\ .$$

Assertion (3.27) follows with Lemma 3 and the differentiation rules (3.21).

For the shape derivative w.r.t. Γ^μ we have to compute

$$d_{\Gamma^\mu}\Big[\|A(f,\mu(\Gamma^\mu)) - y^\delta\|^2_{L^2(\mathbb{R}\times S^1)} + \beta\|R\mu(\Gamma^\mu) - z^\delta\|^2_{L^2(\mathbb{R}\times S^1)} + \alpha|\Gamma^\mu|\,;\ G\Big]\ .$$

Assertion (3.28) follows with Lemma 4, Corollary 1 and the differentiation rules (3.21). □

4. Numerical Results

In this section the introduced algorithm is applied to numerically generated SPECT/CT data. The exact activity and density functions are shown in Figure 1. The piecewise constant activity function f is constructed from a section through a simplified model of a human heart. Figure 1(left) shows

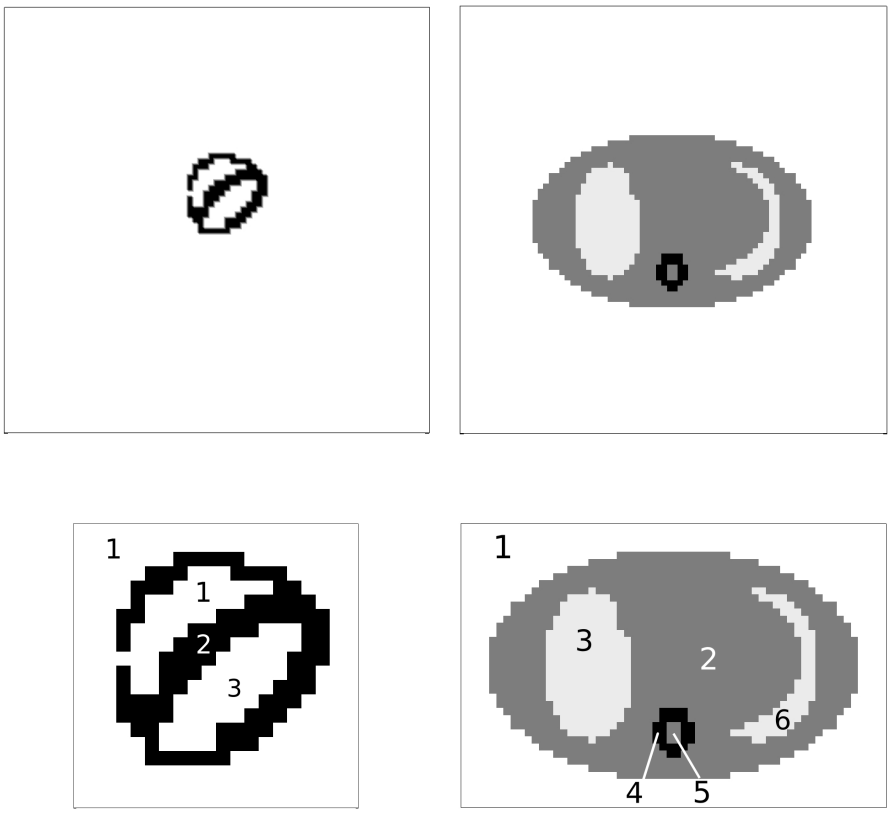

FIGURE 1. Original activity function f and density function μ. Upper row: true proportion; lower row: zoom into image section and numbering of the domains.

the blood supply of the myocardal muscle (no.2) and the two ventricles (no.1 and no.3). The blood supply is interrupted at one point, namely in the outer left area of the myocardal muscle. This point is not reached by the radiopharmaceuticum, hence the left ventricle seems to be 'open'. For that reason, the outer area (no.1) and the upper cardic ventricle have the same number and are modeled as one connected domain in the PC_m-model. For the constrcution of the piecewise constant density function μ a section through a simplified model of a human torso is used: Figure 1(right) shows spine (no.4), spinal canal no.(5), the lungs (no.3 and no.6), the surrounding tissue (no.2) and the exterior (no.1). The tomography data is generated by a Matlab implementation of the Radon operator (1.1) and the attenuated Radon operator (1.2) where 160 samples and 159 directions are used. The generated data is contaminated by noise (additive for CT, multiplicative for SPECT). Simultaneous reconstructions of the functions f and μ together with their singularity sets Γ^f and Γ^μ are achieved by minimizing the Mumford-Shah like functional, cf. (1.4),

$$J(f,\mu,\Gamma^f,\Gamma^\mu) = \|A(f,\mu)-y^\delta\|^2_{L^2(\mathbb{R}\times S^1)}+\beta\|R\mu-z^\delta\|^2_{L^2(\mathbb{R}\times S^1)}+\alpha(|\Gamma^f|+|\Gamma^\mu|)$$

with respect to the space of piecewise constant functions, cf. (2.1). Results of the method described in this paper are presented in Figures 2-6 and

Tables 1-6. The regularization parameter β and α as well as the number of outer iterations are chosen experimentally to produce visionally best looking results. Parameter choice rules, stopping criteria and convergence results are going to be studied in a forthcoming paper. The parameter β is chosen such that there is an approximate equilibrium between the two discrepancy terms. The penalty on the length of the boundary is realized by the parameter α. It might be necessary to adjust the length penalty to quantitatively different lengths of the boundaries Γ^μ and Γ^f. Otherwise it can happen that the parameter is too large for one entity and too small for the other, meaning that especially for high noise level one boundary can get out of hand while the other shrinks more and more and finally vanishes. For that reason, we modify the penalty term from

$$\alpha(|\Gamma^f| + |\Gamma^\mu|) \qquad \text{to} \qquad \alpha_f|\Gamma^f| + \alpha_\mu|\Gamma^\mu|,$$

i.e., we weight each singularity set separately.

As the Mumford-Shah like approach achieves a simultaneous reconstruction of the functions f and μ together with their singularity sets Γ^f and Γ^μ this should be taken into account when assessing the quality of the reconstructions. In a forthcoming theoretical analysis of the regularization properties of this method we are going to use a concept of distance that validates the geometrical difference between the segmented sets as well as the difference in the set-associated function values. For two measurable sets $\Omega_1, \Omega_2 \subset D$ we define the distance

$$d_{L_1}(\Omega_1, \Omega_2) = \|\chi_{\Omega_1} - \chi_{\Omega_2}\|_{L_1(D)} \,. \tag{4.1}$$

As the minimizers of the functional (1.4) are found within the space of piecewise constant functions we define a distance measure as follows.

Definition 1. For $f = \sum_{i=1}^m \alpha_i \chi_{\Omega_i^f} \in \mathrm{PC}_m$ and $g = \sum_{i=1}^m \beta_i \chi_{\Omega_i^g} \in \mathrm{PC}_m$ we define the distance function

$$d_{\mathrm{PC}_m}(f,g) = \min_{\sigma \in S_m} \left\{ \sum_{i=1}^m \left(d_{L_1}(\Omega_i^f, \Omega_{\sigma(i)}^g) + |\alpha_i - \beta_{\sigma(i)}| \right) \right\}$$

where S_m denotes the group of all permutations of the index set $\{1, \dots, m\}$.

As the PC_m-distance depends on a normalization in order to balance the influence of both the geometric error as well as the errors of the function values, we do not use it here. In Tables 1-6 reconstruction errors are given for different error levels ($\delta_{\mathrm{rel}} = 0, 5, 10, 15, 20\%$). We present the d_{L_1}-distance (4.1) for each set and the absolute difference in each coefficient value for both f and μ. Furthermore the relative distances for the sets and the coefficient values are given.

In Table 1 and Figure 2 we supply the results for exact data ($\delta = 0$) without penalty on the length ($\alpha_f = \alpha_\mu = 0$), i.e., we minimize

$$\|A(f,\mu) - y\|^2_{L_2(\mathbb{R}\times S^1} + \beta\|R\mu - z\| \qquad\qquad \beta = 0.01$$

with respect to the space PC_m. This is our reference reconstruction: the contours of the reconstructed density almost coincide with the original one. The largest relative error occurs for $j = 5$ which is the spinal canal and by far the smallest of the sets.

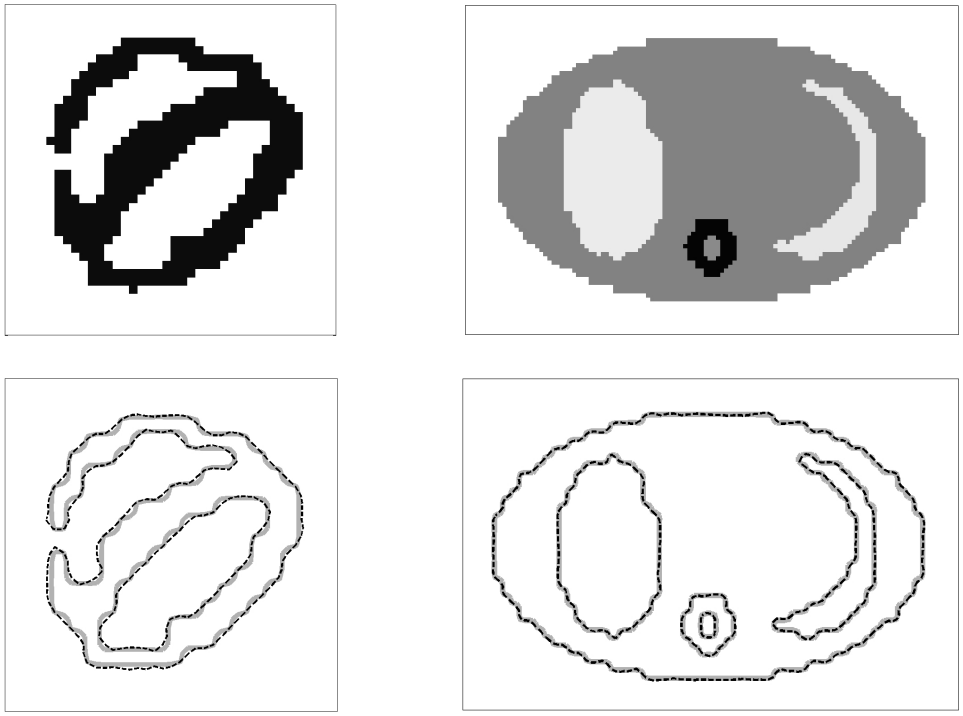

FIGURE 2. 'Best' reconstructions for exact data; upper row: reconstructed activity f and density μ; lower row: contour plot: exact (light grey) and reconstructed (black dashed) contours. Parameter: $\delta = 0$, $\beta = 0.01$, $\alpha_f = \alpha_\mu = 0$, 80 iterations.

j	$d_{L_1}(\Omega_j^f, \Omega_j^{f_{\text{reco}}})$	$d_{L_1}(\Omega_j^f, \Omega_j^{f_{\text{reco}}})/\lvert\Omega_j^f\rvert$	f_j	$f_{\text{reco}\,j}$	$\lvert f_j - (f_{\text{reco}})_j\rvert$
1	7.8125e-6	0.13%	0	4.6922e-11	4.6922e-11
2	1.1230e-5	11.86%	1e-06	0.9504e-06	4.9580e-08
3	3.4180e-6	7.95%	0	-4.5392e-09	4.5392e-09

j	$d_{L_1}(\Omega_j^\mu, \Omega_j^{\mu_{\text{reco}}})$	$d_{L_1}(\Omega_j^\mu, \Omega_j^{\mu_{\text{reco}}})/\lvert\Omega_j^\mu\rvert$	μ_j	$\mu_{\text{reco}\,j}$	$\lvert\mu_j - (\mu_{\text{reco}})_j\rvert$
1	9.0332e-6	0.18%	0	5.4450e-6	5.4450e-6
2	2.1240e-5	2.11%	0.0600	0.0599	6.8860e-4
3	3.6621e-6	1.83%	0.0100	0.0104	4.0080e-4
4	2.1973e-6	8.65%	0.1200	0.1170	3.0431e-3
5	9.7656e-7	16.67%	0.0600	0.0562	3.7557e-3
6	7.3242e-6	10.14%	0.0100	0.0115	1.5071e-3

TABLE 1. Reconstruction errors for f and μ (cp. Figure 2). The errors are given separately for functional and geometrical variables. Parameter values: $\delta = 0$, $\beta = 0.01$, $\alpha_f = \alpha_\mu = 0$, 80 iterations.

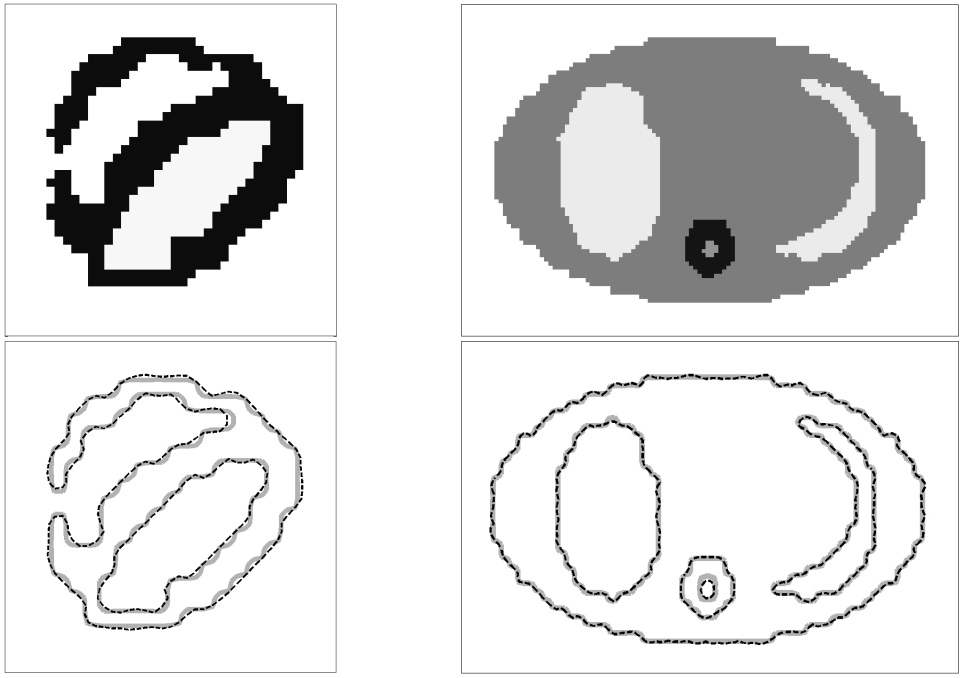

FIGURE 3. Upper row: Reconstructed f and μ from data with 5% relative noise; lower row: contour plot: exact (light grey) and reconstructed (black dashed) contours; parameter $\beta = 1 \cdot 10^{-3}$, $\alpha_f = 1 \cdot 10^{-15}$ and $\alpha_\mu = 1 \cdot 10^{-14}$; 70 iterations.

j	$d_{L_1}(\Omega_j^f, \Omega_j^{f_{\text{reco}}})$	$d_{L_1}(\Omega_j^f, \Omega_j^{f_{\text{reco}}})/\lvert\Omega_j^f\rvert$	f_j	$f_{\text{reco}\,j}$	$\lvert f_j - (f_{\text{reco}})_j\rvert$
1	8.3010e-6	0.14%	0	-1.7364e-10	1.7364e-10
2	1.1475e-5	12.11%	1e-06	0.9406e-06	5.9361e-08
3	3.1738e-6	7.39%	0	3.3640e-08	3.3640e-08

j	$d_{L_1}(\Omega_j^\mu, \Omega_j^{\mu_{\text{reco}}})$	$d_{L_1}(\Omega_j^\mu, \Omega_j^{\mu_{\text{reco}}})/\lvert\Omega_j^\mu\rvert$	μ_j	$\mu_{\text{reco}\,j}$	$\lvert\mu_j - (\mu_{\text{reco}})_j\rvert$
1	1.1719e-5	0.24%	0	-5.4804e-5	5.4804e-5
2	2.8809e-5	2.86%	0.0600	0.0596	3.4061e-4
3	6.5918e-6	3.29%	0.0100	0.0100	2.2707e-5
4	4.6387e-6	18.27%	0.1200	0.1113	7.0893e-3
5	2.1973e-6	37.50%	0.0600	0.0588	1.2027e-3
6	8.0566e-6	11.15%	0.0100	0.0104	3.8009e-4

TABLE 2. Reconstruction errors for f and μ from data with 5% relative noise (cp. Figure 3). The errors are given separately for functional and geometrical variables. parameter values $\beta = 1 \cdot 10^{-3}$, $\alpha_f = 1 \cdot 10^{-15}$ and $\alpha_\mu = 1 \cdot 10^{-14}$; 70 iterations.

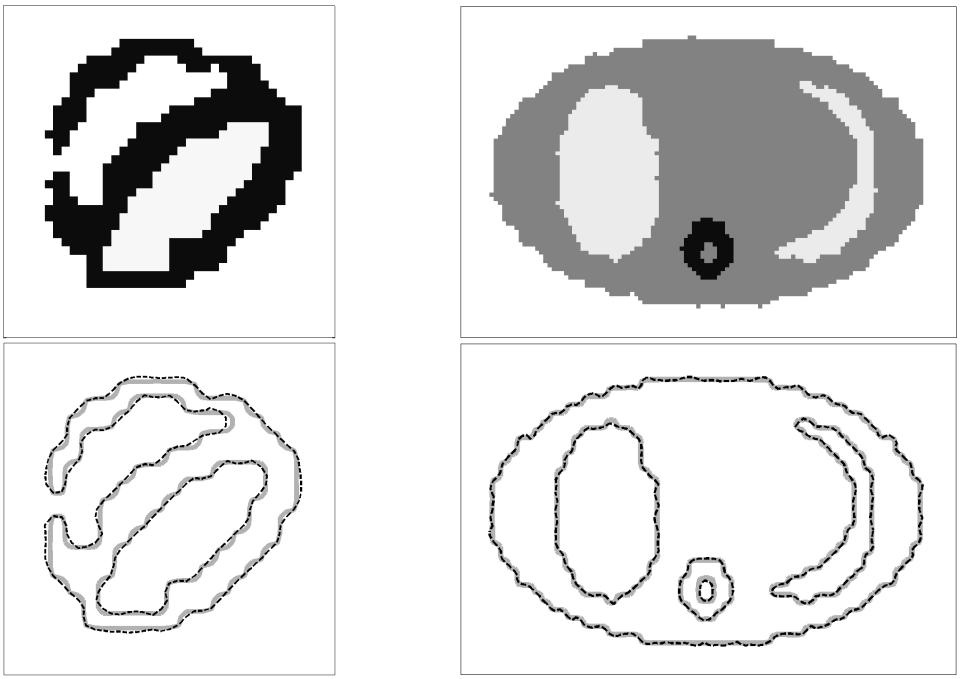

FIGURE 4. Upper row: Reconstructed f and μ from data with 10% relative noise; lower row: contour plot: exact (light grey) and reconstructed (black dashed) contours; parameter $\beta = 1 \cdot 10^{-3}$, $\alpha_f = 1 \cdot 10^{-15}$ and $\alpha_\mu = 1 \cdot 10^{-13}$; 90 iterations.

The spine and the spinal canal are created by an heuristic insert strategy as introduced in [43]. After a certain number of outer iterations the functional derivative of f and μ respectively is checked for local maxima. If there is a significant maximum a new component is inserted at the according position. For low noise levels this works quite fine. However, the decision when to call a maximum of the functional derivative 'significant' asks for proper bounds.

With growing data error ($\delta_{\text{rel}} = 5, 10, 15, 20\%$) the reconstructions (Figures 3-6) change. We discuss this separately for f and μ. The parameter sets are chosen with emphasis on the reconstruction of the blood supply of the myocardal muscle, i.e., the activity function f. The reconstructed heart contours meet the exact contours well for all the given error levels. Especially the disturbance (interruption) of the blood flow is always reconstructed. The tables show that the (geometrical) errors of the reconstructed domains do not change significantly. The errors for the domains Ω_i^f are largest for $\delta = 10\%$, Table 3. The chosen parameter set is not optimal yet.

The change in the reconstruction of the density μ with the error level $\delta_{\text{rel}} = 5, 10, 15, 20\%$ is more visible. The boundaries of the sets oscillate more and more, starting with $\delta = 15\%$. For an error level of 20% the oscillations sometimes split from the original boundary and start to be a set of their own, see Figure 6. In the reconstruction of μ (upper right), the additional set is marked with a magnifier glass. The choice of the parameter

j	$d_{L_1}(\Omega_j^f, \Omega_j^{f_{\text{reco}}})$	$d_{L_1}(\Omega_j^f, \Omega_j^{f_{\text{reco}}})/\lvert\Omega_j^f\rvert$	f_j	$f_{\text{reco}\,j}$	$\lvert f_j - (f_{\text{reco}})_j\rvert$
1	1.0010e-5	0.16%	0	1.2403e-10	1.2403e-10
2	1.3916e-5	14.69%	1e-06	0.9733e-06	0.2667e-07
3	3.9063e-6	9.09%	0	8.0764e-09	8.0764e-09

j	$d_{L_1}(\Omega_j^\mu, \Omega_j^{\mu_{\text{reco}}})$	$d_{L_1}(\Omega_j^\mu, \Omega_j^{\mu_{\text{reco}}})/\lvert\Omega_j^\mu\rvert$	μ_j	$\mu_{\text{reco}\,j}$	$\lvert\mu_j - (\mu_{\text{reco}})_j\rvert$
1	1.4160e-5	0.29%	0	3.1e-5	3.0603e-5
2	3.0518e-5	3.03%	0.0600	0.0604	4.2627e-4
3	5.3711e-6	2.68%	0.0100	0.0100	3.6575e-5
4	5.6152e-6	22.12%	0.1200	0.1113	8.6552e-3
5	2.6855e-6	45.83%	0.0600	0.0439	1.6442e-2
6	8.0566e-6	11.15%	0.0100	0.0108	7.7576e-4

TABLE 3. Reconstruction errors for f and μ from data with 10% relative noise (cp. Figure 4). The errors are given separately for functional and geometrical variables. parameter values $\beta = 1 \cdot 10^{-3}$, $\alpha_f = 1 \cdot 10^{-15}$ and $\alpha_\mu = 1 \cdot 10^{-13}$; 90 iterations.

α_μ for the penalty on the length Γ^μ must be done carefully. On the one hand we want to prevent the oscillation but on the other hand we want the small sets Ω_4^μ, the spine, and Ω_4^μ, the spinal canal, to appear and stay (with α_μ too large the small sets do not show up at all or vanish again). The parameter as chosen in Figures 4-6 already results in a reduced size of the spinal canal, compare also the large relative errors of the according domain in Tables 2-6.

Summary: We presented and tested the Mumford-Shah level-set approach for the simultaneous inversion and segmentation of SPECT/CT data. Activity and density function were modelled as piecewise constant functions. A Mumford-Shah like functional was minimized in turn with respect to the geometry and the functional values. The algorithm was applied to synthetic data with different noise levels and produced good results. So far no regularization results (convergence rate) or parameter choice rules has been presented. This is the subject of a forthcoming paper.

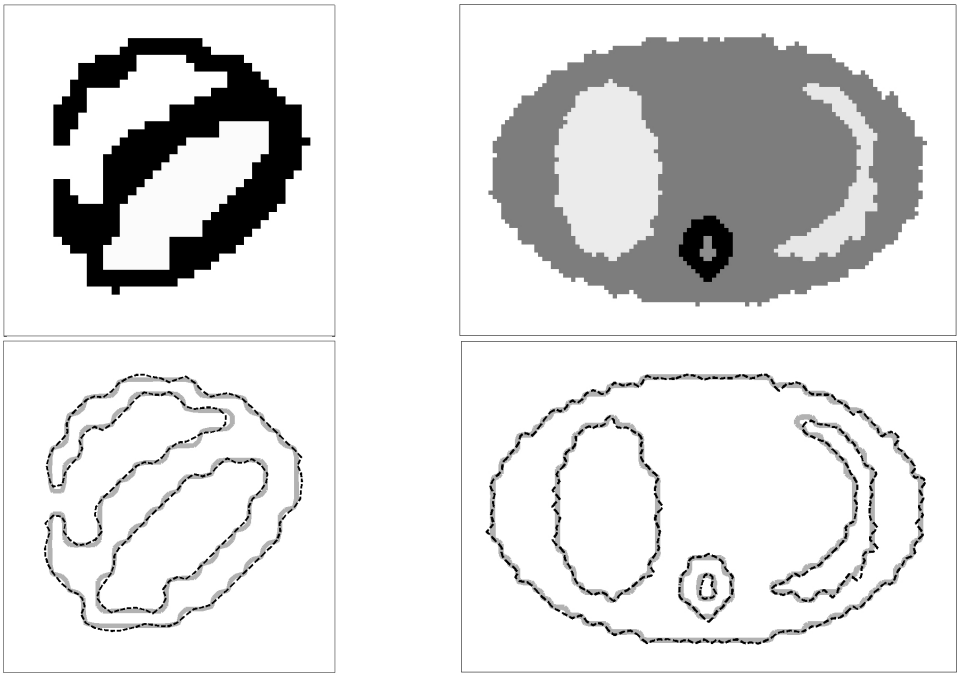

FIGURE 5. Reconstructions from data with 15% relative noise; Upper row: f and μ; lower row: contour plot: exact (light grey) and reconstructed (black dashed) contours. Parameter values $\beta = 1 \cdot 10^{-3}$, $\alpha_f = 1 \cdot 10^{-15}$ and $\alpha_\mu = 1 \cdot 10^{-12}$; 80 iterations.

j	$d_{L_1}(\Omega_j^f, \Omega_j^{f_{\text{reco}}})$	$d_{L_1}(\Omega_j^f, \Omega_j^{f_{\text{reco}}})/\lvert\Omega_j^f\rvert$	f_j	$f_{\text{reco}\,j}$	$\lvert f_j - (f_{\text{reco}})_j\rvert$
1	8.5449e-6	0.14%	0	2.1510e-10	2.1510e-10
2	1.0742e-5	11.34%	1e-06	1.0098e-06	9.7727e-09
3	2.1973e-6	5.11%	0	2.9699e-08	2.9699e-08

j	$d_{L_1}(\Omega_j^\mu, \Omega_j^{\mu_{\text{reco}}})$	$d_{L_1}(\Omega_j^\mu, \Omega_j^{\mu_{\text{reco}}})/\lvert\Omega_j^\mu\rvert$	μ_j	$\mu_{\text{reco}\,j}$	$\lvert\mu_j - (\mu_{\text{reco}})_j\rvert$
1	1.6602e-5	0.34%	0	9.6181e-5	9.6181e-5
2	4.4922e-5	4.45%	0.0600	0.0605	4.8296e-4
3	1.0010e-6	5.00%	0.0100	0.0105	4.8390e-4
4	6.8359e-6	26.92%	0.1200	0.1195	5.3782e-4
5	1.9531e-6	33.33%	0.0600	0.0526	7.3647e-3
6	1.3428e-5	18.58%	0.0100	0.0128	2.7757e-3

TABLE 4. Reconstruction errors for f and μ from data with 15% relative noise (cp. Figure 5). The errors are given separately for functional and geometrical variables. Parameter values: $\beta = 1 \cdot 10^{-3}$, $\alpha_f = 1 \cdot 10^{-15}$ and $\alpha_\mu = 1 \cdot 10^{-12}$, 80 iterations.

j	$d_{L_1}(\Omega_j^f, \Omega_j^{f_{\text{reco}}})$	$d_{L_1}(\Omega_j^f, \Omega_j^{f_{\text{reco}}})/\lvert\Omega_j^f\rvert$	f_j	$f_{\text{reco}\,j}$	$\lvert f_j - (f_{\text{reco}})_j\rvert$
1	9.2773e-06	0.15%	0	2.6146e-11	2.6146e-11
2	1.1963e-05	12.63%	1e-06	9.6282e-07	3.7176e-08
3	2.6855e-06	6.25%	0	2.0609e-08	2.0609e-08

j	$d_{L_1}(\Omega_j^\mu, \Omega_j^{\mu_{\text{reco}}})$	$d_{L_1}(\Omega_j^\mu, \Omega_j^{\mu_{\text{reco}}})/\lvert\Omega_j^\mu\rvert$	μ_j	$\mu_{\text{reco}\,j}$	$\lvert\mu_j - (\mu_{\text{reco}})_j\rvert$
1	2.4414e-5	0.49%	0	9.6179e-5	9.6179e-5
2	5.6396e-5	5.59%	0.0600	0.0608	7.9090e-4
3	1.1475e-5	5.73%	0.0100	0.0111	1.1123e-4
4	7.5684e-6	29.81%	0.1200	0.1104	9.6088e-3
5	1.9531e-6	33.33%	0.0600	0.0354	2.4582e-2
6	1.4648e-5	20.27%	0.0100	0.0117	1.7443e-3
☹	2.4414e-7	∞	0	-0.0783	0.0783

TABLE 5. Reconstruction errors for f and μ from data with 20% relative noise (cp. Figure 6). The errors are given separately for functional and geometrical variables. Parameter values: $\delta = 0.2$, 80 iterations, $\beta = 1 \cdot 10^{-3}$, $\alpha_f = 5 \cdot 10^{-15}$ and $\alpha_\mu = 5 \cdot 10^{-11}$. For μ one extra set grew in the course of iteration.

j	$d_{L_1}(\Omega_j^f, \Omega_j^{f_{\text{reco}}})$	$d_{L_1}(\Omega_j^f, \Omega_j^{f_{\text{reco}}})/\lvert\Omega_j^f\rvert$	f_j	$f_{\text{reco}\,j}$	$\lvert f_j - (f_{\text{reco}})_j\rvert$
1	8.5449e-6	0.14%	0	3.1546e-10	3.1546e-10
2	1.1719e-5	12.37%	1e-06	9.9744e-07	2.5622e-09
3	3.1738e-6	7.39%	0	1.7069e-08	1.7069e-08

j	$d_{L_1}(\Omega_j^\mu, \Omega_j^{\mu_{\text{reco}}})$	$d_{L_1}(\Omega_j^\mu, \Omega_j^{\mu_{\text{reco}}})/\lvert\Omega_j^\mu\rvert$	μ_j	$\mu_{\text{reco}\,j}$	$\lvert\mu_j - (\mu_{\text{reco}})_j\rvert$
1	2.5879e-5	0.5%	0	9.6181e-5	9.6181e-5
2	6.1768e-5	6.12%	0.0600	0.0605	4.8296e-4
3	1.0742e-5	5.37%	0.0100	0.0105	4.8390e-4
4	7.8125e-6	30.77%	0.1200	0.1195	5.3782e-4
5	1.9531e-6	33.33%	0.0600	0.0526	7.3647e-3
6	1.5137e-5	20.95%	0.0100	0.0103	2.7506e-4
☹	5.1270e-6	∞	0	0.0627	0.0627
☹	2.4414e-7	∞	0	-0.0863	0.0863

TABLE 6. Reconstruction errors for f and μ from data with 20% relative noise (no corresponding figure). The errors are given separately for functional and geometrical variables. Parameter values: $\delta = 0.2$, 110 iterations, $\beta = 1 \cdot 10^{-3}$, $\alpha_f = 5 \cdot 10^{-15}$ and $\alpha_\mu = 5 \cdot 10^{-11}$. For μ two extra sets grew in the course of iteration.

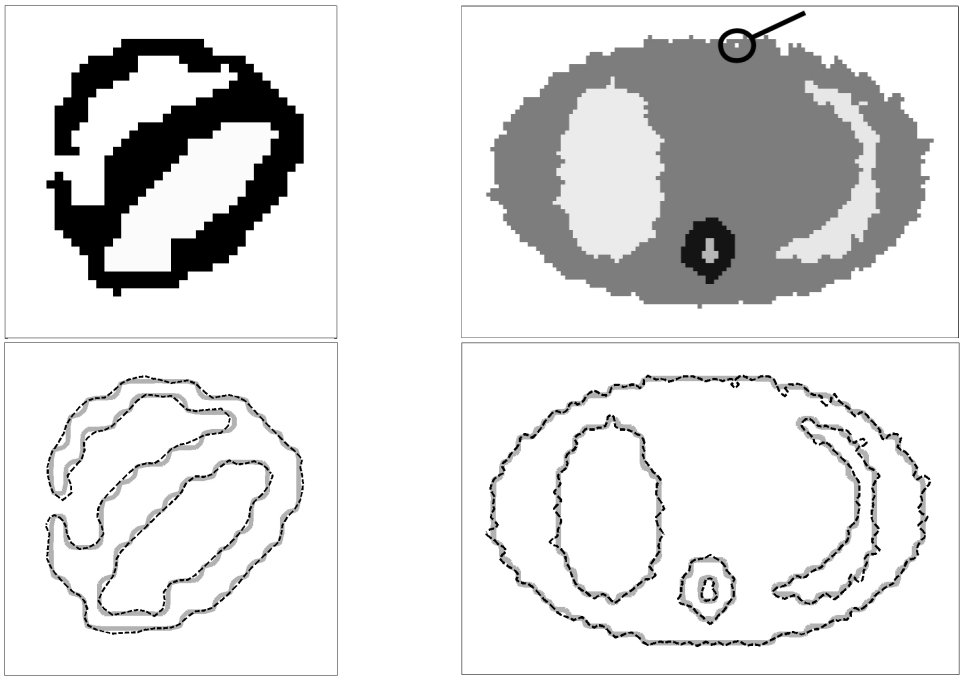

FIGURE 6. Reconstructed f and μ from data with 20% relative noise; parameter $\beta = 1 \cdot 10^{-3}$, $\alpha_f = 5 \cdot 10^{-15}$ and $\alpha_\mu = 5 \cdot 10^{-11}$; 80 iterations. The magnifier glass in the upper right picture indicates an additional set which split from the oscillations of the outer boundary during the course of the iteration.

APPENDIX A

Proposition 3. *Adjoint operators and Fréchet derivative for the attenuated Radon transform $A : L^2(\mathbb{R}^2) \times L^2(\mathbb{R}^2) \to L^2(\mathbb{R} \times S^1)$.*

(1) *Let μ be arbitrary but fixed. In this case, the attenuated Radon transform is a linear operator w.r.t. the variable f and is denoted by A_μ. The adjoint operator A_μ^* applied to a function g and evaluated at $\mathbf{x} \in \mathbb{R}^2$ is given as*

$$A_\mu^* g(\mathbf{x}) = \int_{\omega \in S^1} g(\langle \mathbf{x}, \omega \rangle, \omega) \exp\Big(- \int_{\tau=0}^{\infty} \mu(\mathbf{x} + \tau\omega^\perp)\, d\tau \Big)\, d\omega. \tag{A.1}$$

(2) *Let f be arbitrary but fixed. In this case, the attenuated Radon transform is a nonlinear operator w.r.t. the variable μ and is denoted by A_f. The Fréchet derivative of A_f at the point μ is denoted by $A_f'(\mu)$, see* [16] *for more details. The Fréchet derivative applied to a function $\nu \in L^2(\mathbb{R}^2)$ and evaluated at $(s, \omega) \in (\mathbb{R} \times S^1)$ is given as*

$$\big(A_f'(\mu)\,\nu\big)(s,\omega) = \\ - \int_{\sigma \in \mathbb{R}} \nu(s\omega + \sigma\omega^\perp) \int_{t=-\infty}^{\sigma} f(s\omega + t\omega^\perp) \exp\Big(- \int_{\tau=t}^{\infty} \mu(s\omega + \tau\omega^\perp)\, d\tau \Big)\, dt\, d\sigma. \tag{A.2}$$

(3) *Let f be arbitrary but fixed. The adjoint operator of the Fréchet derivative $A'_f(\mu)$ is denoted by $(A'_f(\mu))^* : L^2(\mathbb{R}\times S^1) \to L^2(\mathbb{R})$. The adjoint operator $(A'_f(\mu))^*$ applied to a function $g \in L^2(\mathbb{R}\times S^1)$ and evaluated at $\mathbf{x} \in \mathbb{R}^2$ is given as*

$$\big((A'_f(\mu))^* g\big)(\mathbf{x}) = \int_{\omega\in S^1} g\big(\langle \mathbf{x},\omega\rangle,\omega\big) \cdot \bigg(\int_{t=-\infty}^{0} f\big(\mathbf{x}+t\omega^\perp\big) \exp\Big(-\int_{\tau=t}^{\infty} \mu\big(\mathbf{x}+\tau\omega^\perp\big)\,d\tau\Big)\,dt\bigg)\,d\omega \quad \text{(A.3)}$$

Proof. The result for the adjoint of the operator A_μ as a linear operator acting on $f \in L^2(\mathbb{R}^2)$ taking values in $L^2(\mathbb{R}\times S^1)$ can be found in [33, Sec. II.6, p. 46ff]. For completeness we present the arguments leading to (A.1).

Using the orthogonal coordinate transformation $(s,t) \mapsto \mathbf{x}(s,t) = s\omega + t\omega^\perp$ and the corresponding inverse transformation $s = \langle \mathbf{x},\omega\rangle$, $t = \langle \mathbf{x},\omega\rangle^\perp$ we obtain

$$\begin{aligned}
&\langle A_\mu f, g\rangle_{L^2(\mathbb{R})\times S^1} \\
&\quad= \int_{\omega\in S^1}\int_{s\in\mathbb{R}}\int_{t\in\mathbb{R}} f(s\omega+t\omega^\perp)\,\exp\Big(-\int_{\tau=t}^{\infty}\mu(s\omega+\tau\omega^\perp)\,d\tau\Big)\,g(s,\omega)\,ds\,d\omega \\
&\quad= \int_{\mathbf{x}\in\mathbb{R}^2} f(\mathbf{x}) \int_{\omega\in S^1} g(\langle \mathbf{x},\omega\rangle,\omega)\,\exp\Big(-\int_{\tau=\langle \mathbf{x},\omega^\perp\rangle}^{\infty}\mu\big(\langle \mathbf{x},\omega\rangle\omega+\tau\omega^\perp\big)\,d\tau\Big)\,d\omega\,d\mathbf{x} \\
&\quad= \int_{\mathbf{x}\in\mathbb{R}^2} f(\mathbf{x}) \int_{\omega\in S^1} g(\langle \mathbf{x},\omega\rangle,\omega)\,\exp\Big(-\int_{\tau=0}^{\infty}\mu(\mathbf{x}+\tau\omega^\perp)\,d\tau\Big)\,d\omega\,d\mathbf{x}
\end{aligned}$$

for all $f \in L^2(\mathbb{R}^2)$ and $g \in L^2(\mathbb{R}, S^1)$. For the last equation we used the transformation $\sigma = \tau + \langle \mathbf{x},\omega^\perp\rangle$ for the integral in the exponential and subsequently changed the notation from σ back to τ. Thus, (A.1) follows.

Differentiating A_f with respect to μ gives

$$\begin{aligned}
&\big(A'_f(\mu)\,\nu\big)(s,\omega) \\
&= -\int_{t\in\mathbb{R}} f(s\omega+t\omega^\perp)\,\exp\Big(-\int_{\tau=t}^{\infty}\mu(s\omega+\tau\omega^\perp)\,d\tau\Big)\int_{\sigma=t}^{\infty}\nu(s\omega+\sigma\omega^\perp)\,d\sigma\,dt \qquad \text{(A.4)} \\
&= -\int_{\sigma\in\mathbb{R}} \nu(s\omega+\sigma\omega^\perp)\int_{t=-\infty}^{\sigma} f(s\omega+t\omega^\perp)\,\exp\Big(-\int_{\tau=t}^{\infty}\mu(s\omega+\tau\omega^\perp)\,d\tau\Big)\,dt\,d\sigma. \qquad \text{(A.5)}
\end{aligned}$$

For the derivation of (A.3) we use (A.5). We find

$$\begin{aligned}
\big\langle g, A_f'(\mu)\,\nu\big\rangle_{L^2(\mathbb{R}\times S^1)} &= -\int_{s\in\mathbb{R}}\int_{\omega\in S^1} g(s,\omega)\int_{\sigma\in\mathbb{R}} \nu(s\omega+\sigma\omega^\perp)\\
&\quad\cdot\Big(\int_{t=-\infty}^{\sigma} f(s\omega+t\omega^\perp)\,\exp\Big(-\int_{\tau=t}^{\infty}\mu(s\omega+\tau\omega^\perp)\,d\tau\Big)\,dt\Big)\,d\sigma\,d\omega\,ds\\
&= \int_{\mathbf{x}\in\mathbb{R}^2}\nu(\mathbf{x})\int_{\omega\in S^1} g\big(\langle\mathbf{x},\omega\rangle,\omega\big)\\
&\quad\cdot\Big(\int_{t=-\infty}^{\langle\mathbf{x},\omega^\perp\rangle} f\big(\langle\mathbf{x},\omega\rangle\omega+t\omega^\perp\big)\exp\Big(-\int_{\tau=t}^{\infty}\mu\big(\langle\mathbf{x},\omega\rangle\omega+\tau\omega^\perp\big)\,d\tau\Big)\,dt\Big)\,d\omega\,d\mathbf{x}\\
&= \int_{\mathbf{x}\in\mathbb{R}^2}\nu(\mathbf{x})\int_{\omega\in S^1} g\big(\langle\mathbf{x},\omega\rangle,\omega\big)\\
&\quad\cdot\Big(\int_{t=-\infty}^{0} f\big(\mathbf{x}+t\omega^\perp\big)\exp\Big(-\int_{\tau=t}^{\infty}\mu\big(\mathbf{x}+\tau\omega^\perp\big)\,d\tau\Big)\,dt\Big)\,d\omega\,d\mathbf{x}.
\end{aligned}$$

Here we used the orthogonal coordinate transformation $(s,\sigma)\mapsto\mathbf{x}(s,\sigma)=s\omega+\sigma\omega^\perp$ with the inverse transformation given by $s=\langle\mathbf{x},\omega\rangle$, $\sigma=\langle\mathbf{x},\omega^\perp\rangle$ and we transformed the half-line integrals to the domain $(-\infty,0)$ and (t,∞) respectively. From this, (A.3) follows.

□

References

[1] Gilles Aubert and Pierre Kornprobst. *Mathematical problems in image processing.* Springer-Verlag, New York, 2002. Partial differential equations and the calculus of variations, With a foreword by Olivier Faugeras.

[2] Hend Ben Ameur, Martin Burger, and Benjamin Hackl. Level set methods for geometric inverse problems in linear elasticity. *Inverse Problems*, 20(3):673–696, 2004.

[3] Andreas K. Buck, Stephan Nekolla, Sibylle Ziegler, Ambros Beer, Bernd J. Krause, Ken Herrmann, Klemens Scheidhauer, Hans-Juergen Wester, Ernst J. Rummeny, Markus Schwaiger, and Alexander Drzezga. SPECT/CT. *The Journal of Nuclear Medicine*, 49(8):1305–1319, August 2008.

[4] J.K. Bucsko. SPECT/CT - The Future is Clear. *Radiology Today*, 5(24), 2004.

[5] Martin Burger. Levenberg-Marquardt level set methods for inverse obstacle problems. *Inverse Problems*, 20(1):259–282, 2004.

[6] Vicent Caselles, Francine Catté, Tomeu Coll, and Françoise Dibos. A geometric model for active contours in image processing. *Numer. Math.*, 66(1):1–31, 1993.

[7] Antonin Chambolle. Image segmentation by variational methods: Mumford and Shah functional and the discrete approximations. *SIAM J. Appl. Math.*, 55(3):827–863, 1995.

[8] T. F. Chan and L. A. Vese. Image segmentation using level sets and the piecewise constant Mumford-Shah model. UCLA CAM Report 00-14, University of California , Los Angeles, 2000.

[9] T. F. Chan and L. A. Vese. A level set algorithm for minimizing the Mumford-Shah functional in image processing. UCLA CAM Report 00-13, University of California , Los Angeles, 2000.

[10] T. F. Chan and L. A. Vese. Active contours without edges. *IEEE Trans. Image Processing*, 10(2):266–277, 2001.

[11] Tony F. Chan and Xue-Cheng Tai. Level set and total variation regularization for elliptic inverse problems with discontinuous coefficients. *J. Comput. Phys.*, 193(1):40–66, 2004.

[12] Tony F. Chan and Luminita A. Vese. Active contours without edges. *IEEE Trans. Image Process.*, 10(2):266–277, 2001.

[13] L. D. Cohen and R. Kimmel. Global minimum for active contour models: a minimum path approach. *International Journal of Computer Vision*, 24(1):57–78, 1997.

[14] Dominique Delbeke, R.Edward Coleman, Milton J. Guiberteau, Manuel L. Brown, Henry D. Royal, Barry A. Siegel, David W. Townsend, Lincoln L. Berland, J.Anthony Parker, George Zubal, and Valerie Cronin. Procedure Guideline for SPECT/CT Imaging. *The Journal of Nuclear Medicine*, 47(7):1227–1234, July 2006.

[15] M. C. Delfour and J.-P. Zolésio. *Shapes and geometries*. Society for Industrial and Applied Mathematics (SIAM), Philadelphia, PA, 2001. Analysis, differential calculus, and optimization.

[16] Volker Dicken. A new approach towards simultaneous activity and attenuation reconstruction in emission tomography. *Inverse Probl.*, 15(4):931–960, 1999.

[17] Oliver Dorn. Shape reconstruction in scattering media with voids using a transport model and level sets. *Can. Appl. Math. Q.*, 10(2):239–275, 2002.

[18] Oliver Dorn, Eric L. Miller, and Carey M. Rappaport. A shape reconstruction method for electromagnetic tomography using adjoint fields and level sets. *Inverse Problems*, 16(5):1119–1156, 2000. Electromagnetic imaging and inversion of the Earth's subsurface.

[19] J.-P. Guillement, F. Jauberteau, L. Kunyansky, R. Novikov, and R. Trebossen. On single-photon emission computed tomography imaging based on an exact formula for the nonuniform attenuation correction. *Inverse Probl.*, 18(6), 2002.

[20] M. Hintermüller and W. Ring. A level set approach for the solution of a state constrained optimal control problem. Technical Report 212, Special Research Center on Optimization and Control, University of Graz, Austria, 2001. to appear in Numerische Mathematik.

[21] M. Hintermüller and W. Ring. An inexact Newton-CG-type active contour approach for the minimization of the Mumford-Shah functional. *J. Math. Imag. Vis.*, 20(1–2):19–42, 2004.

[22] Michael Hintermüller and Wolfgang Ring. A second order shape optimization approach for image segmentation. *SIAM J. Appl. Math.*, 64(2):442–467, 2003.

[23] Kazufumi Ito, Karl Kunisch, and Zhilin Li. Level-set function approach to an inverse interface problem. *Inverse Problems*, 17(5):1225–1242, 2001.

[24] S. Jehan-Besson, M. Barlaud, and G. Aubert. DREAM^{2}S: Deformable regions driven by an Eulerian accurate minimization method for image and video segmentation. November 2001.

[25] S. Jehan-Besson, M. Barlaud, and G. Aubert. Video object segmentation using Eulerian region-based active contours. In *International Conference on Computer Vision, Vancouver*, July 2001.

[26] M. Kass, A. Witkin, and D. Terzopoulos. Snakes; active contour models. *Int. J. of Computer Vision*, 1:321–331, 1987.

[27] H. Kudo and H. Nakamura. A new appraoch to SPECT attenuation correction without transmission maesurements. *Nuclear Science Symposium Conference Record*, 2:13/58–13/62, 2000.

[28] Leonid A. Kunyansky. A new SPECT reconstruction algorithm based on the Novikov explicit inversion formula. *Inverse Probl.*, 17(2):293–306, 2001.

[29] A. Litman, D. Lesselier, and F. Santosa. Reconstruction of a two-dimensional binary obstacle by controlled evolution of a level-set. *Inverse Problems*, 14:685–706, 1998.

[30] M. Mancas, B. Gosselin, and B. Macq. Segmentation using a region-growing thresholding. In E. R. Dougherty, J. T. Astola, and K. O. Egiazarian, editors, *Society of Photo-Optical Instrumentation Engineers (SPIE) Conference Series*, volume 5672 of *Presented at the Society of Photo-Optical Instrumentation Engineers (SPIE) Conference*, pages 388–398, March 2005.

[31] David Mumford and Jayant Shah. Optimal approximations by piecewise smooth functions and associated variational problems. *Comm. Pure Appl. Math.*, 42(5):577–685, 1989.

[32] F. Natterer. Inversion of the attenuated Radon transform. *Inverse Probl.*, 17(1):113–119, 2001.

[33] F. Natterer. *The Mathematics of Computerized Tomography*, volume 32 of *Classics in Applied Mathematics*. Society for Industrial and Applied Mathematics (SIAM), Philadelphia, PA, 2001. Reprint of the 1986 original.

[34] Frank Natterer. Determination of tissue attenuation in emission tomography of optically dense media. *Inverse Probl.*, 9(6):731–736, 1993.

[35] Frank Natterer. *The mathematics of computerized tomography*. Classics in Applied Mathematics. 32. Philadelphia, PA: SIAM. xvii, 222 p., 2001.

[36] Roman G. Novikov. An inversion formula for the attenuated X-ray transformation. *Ark. Mat.*, 40(1):145–167, 2002.

[37] Stanley J. Osher and Ronald P. Fedkiw. *Level Set Methods and Dynamic Implicit Surfaces*. Springer Verlag, New York, 2002.

[38] Stanley J. Osher and Fadil Santosa. Level set methods for optimization problems involving geometry and constraints. I. Frequencies of a two-density inhomogeneous drum. *J. Comput. Phys.*, 171(1):272–288, 2001.

[39] N. Paragios and R. Deriche. Geodesic active regions: a new paradigm to deal with frame partition problems in computer vision. *International Journal of Visual Communication and Image Representation, Special Issue on Partial Differential Equations in Image Processing, Computer Vision and Computer Graphics*, 2001. To appear in 2001.

[40] G.N. Ramachandran and A.V. Lakshminarayanan. Three-dimensional reconstruction from radiographs and electron micrographs: Application of convolutions instead of fourier transforms. *PNAS*, 68(9):2236–2240, September 1971.

[41] R. Ramlau, R. Clackdoyle, R. Noo, and G. Bal. Accurate attenuation correction in SPECT imaging using optimization of bilinear functions and assuming an unknown spatially-varying attenuation distribution. *ZAMM, Z. Angew. Math. Mech.*, 80(9):613–621, 2000.

[42] Ronny Ramlau. TIGRA – an iterative algorithm for regularizing nonlinear ill-posed problems. *Inverse Probl.*, 19(2):433–465, 2003.

[43] Ronny Ramlau and Wolfgang Ring. A Mumford–Shah level-set approach for the inversion and segmentation of X-ray tomography data. *J. Comput. Phys.*, 221(2):539–557, 2007.

[44] F. Santosa. A level-set approach for inverse problems involving obstacles. *ESAIM: Control, Optimization and Calculus of Variations*, 1:17–33, January 1996.

[45] Guillermo Sapiro. *Geometric partial differential equations and image analysis*. Cambridge University Press, Cambridge, 2001.

[46] J. A. Sethian. *Level set methods and fast marching methods*. Cambridge University Press, Cambridge, second edition, 1999. Evolving interfaces in computational geometry, fluid mechanics, computer vision, and materials science.

[47] L.A. Shepp and B.F. Logan. The Fourier reconstruction of a head section. *IEEE Trans. Nucl. Sci*, pages 21–43, 1974.

[48] J. Sokołowski and J-P. Zolésio. *Introduction to shape optimization*. Springer-Verlag, Berlin, 1992. Shape sensitivity analysis.

[49] Demetri Terzopoulos. Deformable models: classic, topology-adaptive and generalized formulations. In *Geometric level set methods in imaging, vision, and graphics*, pages 21–40. Springer, New York, 2003.

[50] Oleh Tretiak and Charles Metz. The exponential Radon transform. *SIAM J. Appl. Math.*, 39:341–354, 1980.

[51] A. Tsai, A. Yezzi, and A. S. Willsky. Curve evolution implementation of the Mumford-Shah functional for image segementation, denoising, interpolation, and magnification. *IEEE Transactions on image processing*, 10(8):1169–1186, 2001.

[52] Joachim Weickert. *Anisotropic Diffusion in Image Processing*. European Consortium for Mathematics in Industry. Teubner, Stuttgart, Leipzig, 1998.

[53] A. Welch, R. Clack, F. Natterer, and G.T. Herman. Toward accurate attenuation correction in spect without transmission measurements. *IEEE Trans. Med. Imaging*, 16(5):532–541, 1997.

* Johann Radon Institut for Applied and Computational Mathematics, Austrian Academy of Sciences, Altenbergerstrasse 69, A-4040 Linz, Austria.
E-mail address: esther.klann@oeaw.ac.at

† Industrial Mathematics Institute Johannes Kepler University Linz Altenbergerstrasse 69 A-4040 Linz, Austria.
E-mail address: ronny.ramlau@jku.at

♯ Institut für Mathematik, Universität Graz, Heinrichstrasse 36, A-8010 Graz, Austria.
E-mail address: wolfgang.ring@uni-graz.at